AD-A117 427 MCDONNELL DOUGLAS RESEARCH LABS ST LOUIS MO F/G 20/4
VISCOUS FLOWFIELDS INDUCED BY THREE-DIMENSIONAL LIFT JETS IN GR--ETC(U)
UNCLASSIFIED JUL 80 W W BOWER, G R PETERS N00014-79-C-0635
MDC-Q0768 NL

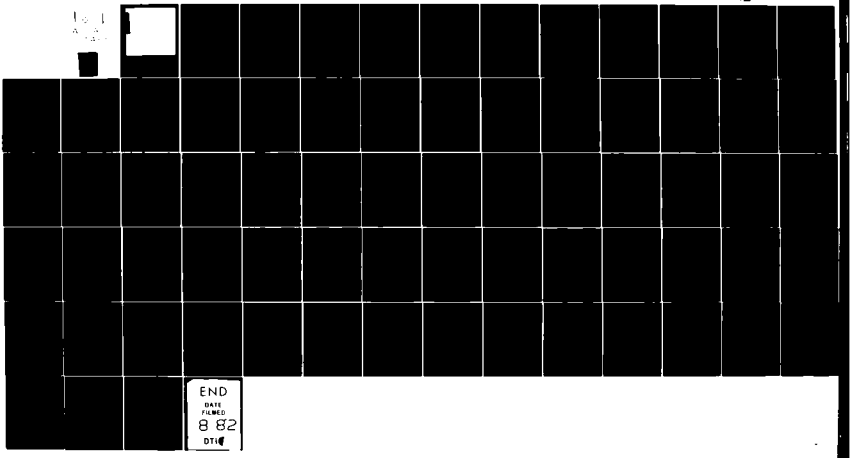

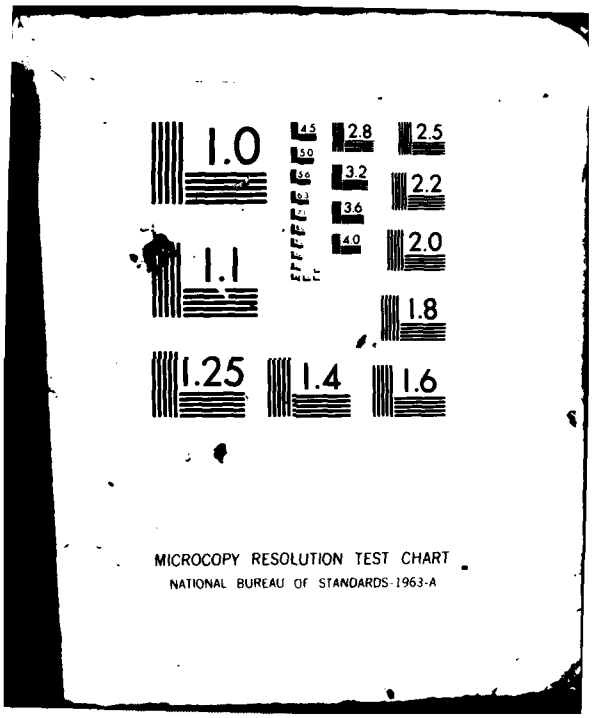
1.0
1.1
1.25
1.4
1.6
1.8
2.0
2.2
2.5
2.8
3.2
3.6
4.0
4.5
5.0
5.6
6.3
MICROCOPY RESOLUTION TEST CHART
NATIONAL BUREAU OF STANDARDS-1963-A

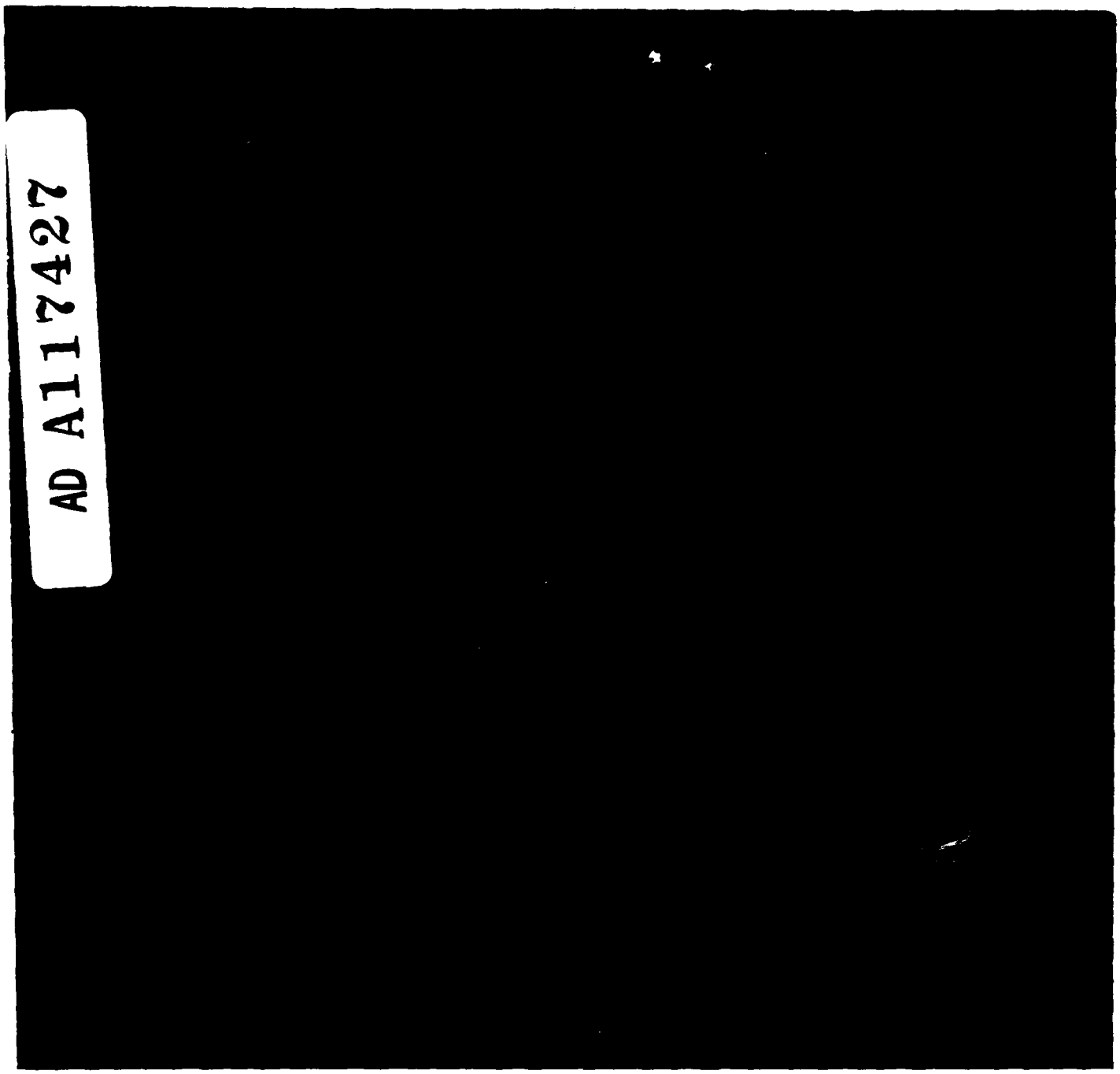

MCDONNELL DOUGLAS RESEARCH LABORATORIES

MCDONNELL DOUGLAS CORPORATION

Change of Address

Organizations receiving reports on the initial distribution list should confirm correct address. This list is located at the end of the report. Any change of address or distribution should be conveyed to the Office of Naval Research, Code 211, Arlington, VA 22217.

Disposition

When this report is no longer needed, it may be transmitted to other organizations. Do not return it to the originator or the monitoring office.

Disclaimer

The findings and conclusions contained in this report are not to be construed as an official Department of Defense or Military Department position unless so designated by other official documents.

Reproduction

Reproduction in whole or in part is permitted for any purpose of the United States Government.

UNCLASSIFIED

SECURITY CLASSIFICATION OF THIS PAGE (When Data Entered)

REPORT DOCUMENTATION PAGE		READ INSTRUCTIONS BEFORE COMPLETING FORM
1. REPORT NUMBER	2. GOVT ACCESSION NO. AD-A117427	3. RECIPIENT'S CATALOG NUMBER
4. TITLE (and Subtitle) VISCOUS FLOWFIELDS INDUCED BY THREE-DIMENSIONAL LIFT JETS IN GROUND EFFECT		5. TYPE OF REPORT & PERIOD COVERED Final Technical Report 1 July 1979 - 30 June 1980
		6. PERFORMING ORG. REPORT NUMBER
7. AUTHOR(s) W. W. Bower G. R. Peters		8. CONTRACT OR GRANT NUMBER(s) N00014-79-C-0635
9. PERFORMING ORGANIZATION NAME AND ADDRESS McDonnell Douglas Research Laboratories McDonnell Douglas Corporation St. Louis, MO 63166		10. PROGRAM ELEMENT, PROJECT, TASK AREA & WORK UNIT NUMBERS
11. CONTROLLING OFFICE NAME AND ADDRESS Office of Naval Research Vehicle Technology Program, Code 211 800 N. Quincy Street, Arlington, VA 22217		12. REPORT DATE 1 July 1980
		13. NUMBER OF PAGES
14. MONITORING AGENCY NAME & ADDRESS(if different from Controlling Office)		15. SECURITY CLASS. (of this report) Unclassified
		15a. DECLASSIFICATION DOWNGRADING SCHEDULE

16. DISTRIBUTION STATEMENT (of this Report)

Approved for public release; distribution unlimited

17. DISTRIBUTION STATEMENT (of the abstract entered in Block 20, if different from Report)

18. SUPPLEMENTARY NOTES

19. KEY WORDS (Continue on reverse side if necessary and identify by block number)

VTOL lift jet
Ground effect
Viscous
Turbulence modeling
Finite-difference methods

20. ABSTRACT (Continue on reverse side if necessary and identify by block number)

An important consideration for VTOL aircraft design is the aerodynamic interaction between the lift jets and the ground plane. In an effort to predict this phenomenon for two jets, a finite-difference solution of the three-dimensional conservation equations of fluid mechanics, in combination with a turbulence model, has been developed for the case of incompressible flow. The solution technique is applied to the normal and oblique impingement of equal- and unequal-strength jets in ground effect with fountain formation. Fluid properties that characterize the flowfields are presented, and computed

DD FORM 1 JAN 73 1473 EDITION OF 1 NOV 65 IS OBSOLETE

UNCLASSIFIED

SECURITY CLASSIFICATION OF THIS PAGE (When Data Entered)

results are compared with data for the ground plane pressure distribution, fountain flow direction, wall-jet properties, and stagnation line shape.

PREFACE

This final technical report is an account of the work completed at the McDonnell Douglas Research Laboratories (MDRL) on Viscous Flowfields Induced by Three-Dimensional Lift Jets in Ground Effect, Contract No. N00014-79-C-0635, from 1 July 1979 to 30 June 1980. The work was done in the Flight Sciences Department, managed by Dr. R. J. Hakkinen. The principal investigator was Dr. W. W. Bower. The program monitor was Dr. R. E. Whitehead, Office of Naval Research (ONR), Arlington, VA.

TABLE OF CONTENTS

LIST OF ILLUSTRATIONS

LIST OF TABLES

1. INTRODUCTION

In recent years, considerable effort has been devoted to the aerodynamics of vertical-takeoff-and-landing (VTOL) aircraft in ground effect. In this mode of operation, which is associated with takeoff, hover, and landing, there is a strong interaction between the lift-jet flow and the surrounding fuselage and ground surfaces. The resulting interference forces affect significantly the aircraft performance. Because of the increased complexity of the ground-effect flowfield, which is characterized by three-dimensional, turbulent, interacting free jets and wall jets, these forces cannot be predicted by analytical procedures developed to describe the external aerodynamics of conventional-takeoff-and-landing aircraft without extensive modification.

Attempts to predict these flows currently rely on a so-called modular analysis, such as the techniques described in References 1 and 2. With these approaches, the complete flowfield is divided into components, specifically the free jets, the wall jets, and the upwash formed through the collision of the opposing wall jets. The components are modeled using a separate system of equations for each zone. The solutions are then iteratively pieced together to provide a description of the total region of interest. One shortcoming of this approach is the difficulty frequently encountered in accurately patching together the component solutions. In addition, the modular analysis techniques rely heavily on experimental data which are frequently configuration dependent.

In an effort to describe jet impingement flows from a more general and fundamental point of view, MDRL has performed work under ONR support on solution of the Reynolds-averaged Navier-Stokes and turbulence model equations applied to these flowfields. Initially, calculations were made for an isolated planar lift jet discharging from a simulated fuselage undersurface in ground proximity for both incompressible and compressible conditions. This work, which is reported in Reference 3, provides accurate predictions of the fuselage undersurface and ground-plane pressure distributions, illustrating their variation with Reynolds number and jet height above ground. In addition, the experience gained in the development of the flowfield model and the numerical solution scheme for two-dimensional flow formed the basis for

extending the analysis to the considerably more complex three-dimensional jet impingement configurations.

The geometry of interest in the present study consists of two interacting, initially axisymmetric jets with fountain formation; the geometry is shown schematically in Figure 1 for the general case of inclined impingement. The jets exit from two axisymmetric nozzles, each with diameter D, whose centerlines are separated by a spacing S. The distance from the nozzle exit plane to the midpoint between the intercepts of the geometric jet centerlines with the ground plane is denoted by H_c, and the jet inclination angle relative to the ground plane is denoted by α.

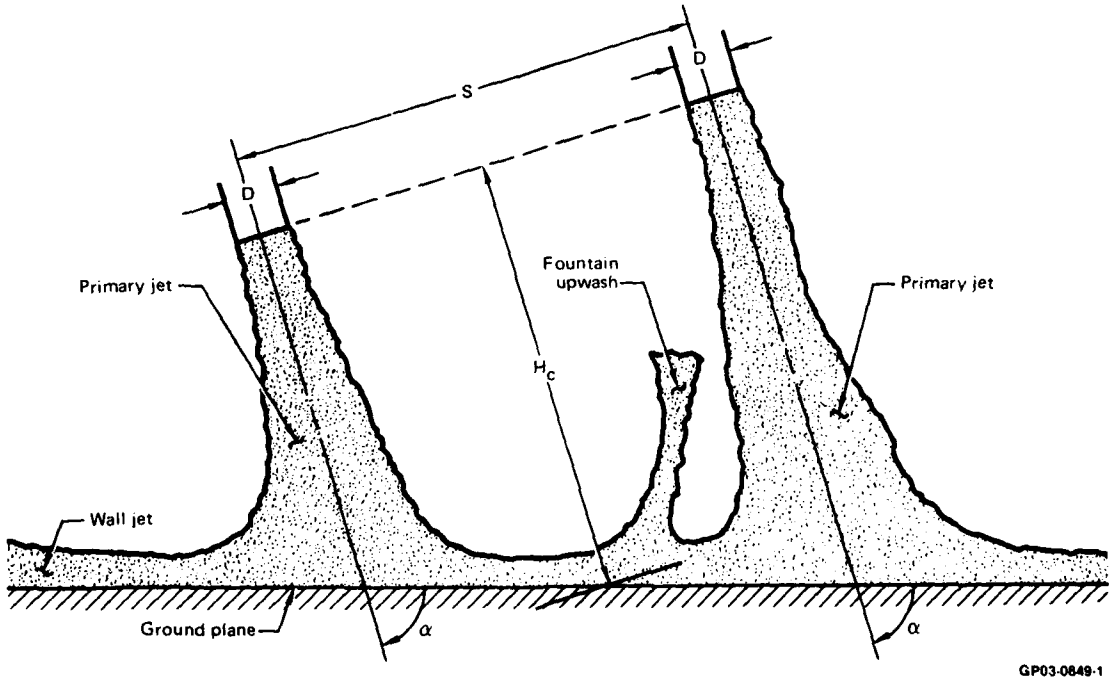

Figure 1. Sketch of inclined jet impingement with fountain formation.

The impingement of the two parallel jets on the ground creates two adjacent wall jets which spread radially and collide to form a fountain upwash flow that is directed away from the ground. The flow properties of the fountain are determined by the geometric parameters of the configuration (S, H_c, and α) and the relative strengths of the two primary jets. For large values of nozzle centerline spacing (typically S/D > 10), the upwash characteristics can be predicted from the wall-jet properties, which in turn can be correlated with the nozzle exit flow conditions. However, for closer centerline spacing, this may not be the case since the fountain flow can be affected by its interaction with the primary jets. This situation becomes more pronounced as the jet centerline spacing S and height above ground H_c are decreased.

In VTOL aircraft design, close nozzle spacing is of interest since it can reduce weight requirements. Consequently, dual-jet impingement with fountain formation for S/D < 10 is a relevant research problem. An approximate method for modeling close-jet phenomena using a modular approach based on empirical data and global conservation-law constraints has been reported in Reference 4 for the range $2 \leq S/D \leq 6$. The flow models for the various zones are coupled through their dependence upon the upstream behavior of the prior region and the downstream position of the opposing jet. The technique provides the flow properties of engineering interest, but, as pointed out by the authors (Refernce 4), further refinement requires a more extensive experimental data base and a better resolution of the influence of turbulence-induced static pressure variations.

The analytical approach adopted in the current study for the dual-jet impingement analysis is a solution of the time-averaged Navier-Stokes equations, with a complementary turbulence model, for steady, incompressible flow. The conservation equations are solved in terms of scalar and vector potential functions and vorticity using a second-order-accurate finite-difference algorithm. Flowfield characteristics gained from such a study can be used to evaluate and improve engineering models of the fountain flow (References 1, 2, and 4) that are the basis for predicting VTOL aircraft performance in ground effect.

This report describes the flowfield model, the numerical solution technique, and representative results. The latter include flowfield properties for the following dual-jet impingement configurations, which are of interest in the current study: equal-strength jets with normal impingement, unequal-strength jets with normal impingement, equal-strength jets with inclined impingement, and unequal-strength jets with inclined impingement. The direction of future MDRL work in the calculation of three-dimensional jet impingement flowfields under ONR contract N00014-80-C-0454 is discussed.

2. THE FLOWFIELD MODEL

In this section, the governing equations are presented which are used to describe the turbulent, incompressible, steady flow of the three-dimensional impinging jet configurations of interest. The complete time-averaged Navier-Stokes equations and a one-equation turbulence model are given in terms of the velocity components and pressure, and then they are rewritten in terms of vorticity, scalar, and vector potential functions. Boundary conditions are defined for the interacting jets with fountain formation.

2.1 The Governing Equations

The time-averaged continuity and momentum (Navier-Stokes) equations for steady incompressible flow are given below in tensor notation for a space-fixed reference through which the fluid moves.

Conservation of mass:

$$\frac{\partial \bar{u}_j}{\partial x_j} = 0 \tag{2-1}$$

Conservation of momentum in the i^{th} direction:

$$\rho \frac{\partial (\bar{u}_j \bar{u}_i)}{\partial x_j} + \frac{\partial \bar{p}}{\partial x_i} - \frac{\partial}{\partial x_j} (\bar{\tau}_{ij} - \rho \overline{u_i' u_j'}) = 0 \tag{2-2}$$

The conventional notation is used in which ρ is the density, u_i the velocity component in the i^{th} direction, p the static pressure, and τ_{ij} the shear stress in the i^{th} direction on a surface normal to the j^{th} direction.

The previous equations were derived using Reynolds decomposition in which a general flow variable ϕ is expressed as the sum of a time-averaged component $\bar{\phi}$ and a fluctuating component ϕ', $\phi = \bar{\phi} + \phi'$. The result is a system of time-averaged conservation equations which have the same form as the

instantaneous conservation equations with the exception of the Reynolds stress term $-\rho\ \overline{u_i' u_j'}$.

In order to obtain a closed system of equations, the Reynolds stress term must be related to the time-averaged quantities that describe the mean flow. In the present work, this is accomplished using the one-equation incompressible turbulence model of Glushko, Reference 5. With this approach, the effective shear-stress term in Equation (2-2) is represented by

$$\bar{\tau}_{ij} - \rho\ \overline{u_i' u_j'} = \mu_{eff}\left(\frac{\partial \bar{u}_i}{\partial x_j} + \frac{\partial \bar{u}_j}{\partial x_i}\right) - \frac{2}{3}\,\delta_{ij}\rho k, \tag{2-3}$$

where μ_{eff} is the effective viscosity (the sum of the molecular and turbulent components, $\mu_{eff} = \mu + \mu_t$) and k is the turbulent kinetic energy. The latter is computed from the following transport equation:

$$\rho\,\frac{\partial(\bar{u}_j k)}{\partial x_j} = \mu_t\left(\frac{\partial \bar{u}_i}{\partial x_j} + \frac{\partial \bar{u}_j}{\partial x_i}\right)\frac{\partial \bar{u}_i}{\partial x_j} - \frac{2}{3}\,\delta_{ij}\rho k\,\frac{\partial \bar{u}_i}{\partial x_j}$$

$$+ \frac{\partial}{\partial x_i}\left[\mu\varepsilon(\lambda\bar{r})\,\frac{\partial k}{\partial x_i}\right] + \mu\,\frac{\partial^2 k}{\partial x_j^{\,2}} - \frac{\mu C k}{L^2}\left[1 + \varepsilon(\lambda\bar{r})\right]. \tag{2-4}$$

In the Glushko model, the turbulent component of the effective viscosity is given by

$$\mu_t = \mu\varepsilon(\bar{r}), \tag{2-5}$$

where $\varepsilon(\bar{r})$ is computed from the relation

$$\varepsilon(\bar{r}) = H(\bar{r})\alpha\bar{r}. \tag{2-6}$$

In Equation (2-6), $\bar{r}$ is the Reynolds number of the turbulence based on the length scale of the turbulence L,

$$\bar{r} = \frac{\sqrt{k}\, L}{\nu} \; ; \tag{2-7}$$

α is a constant with value 0.2; and $H(\bar{r})$ is a function defined by

$$H(\bar{r}) = - \begin{cases} \dfrac{\bar{r}}{\bar{r}_o} & 0 \leq \dfrac{\bar{r}}{\bar{r}_o} < 0.75 \\ \dfrac{\bar{r}}{\bar{r}_o} - \left(\dfrac{\bar{r}}{\bar{r}_o} - 0.75 \right)^2 & 0.75 \leq \dfrac{\bar{r}}{\bar{r}_o} < 1.25 \\ 1 & 1.25 \leq \dfrac{\bar{r}}{\bar{r}_o} < \infty \end{cases} , \tag{2-8}$$

where $\bar{r}_o = 110$. With the turbulent kinetic energy computed from Equation (2-4), the turbulent component of the effective viscosity can be evaluated using Equations (2-5) through (2-8). The effective viscosity in turn determines the shear stress, Equation (2-3), appearing in the time-averaged momentum equation.

Although the partial differential equations that describe the flowfield are written in terms of u_i, they are not solved for the velocity components. Rather, the equations are solved in terms of scalar and vector potential functions and vorticity using an approach proposed by Aregbesola and Burley, Reference 6. In this technique, which is analogous to the stream-function/vorticity approach frequently adopted in two-dimensional problems, the pressure is eliminated from the momentum equations in the formulation of a vorticity transport equation. The pressure field is then computed from a Poisson equation, also derived from the component momentum equations.

Consider first the equation for the conservation of mass. To identically satisfy the continuity condition, Equation (2-1), a scalar potential Φ and a vector potential A_i are introduced which are related to the velocity field by the following expression:

$$u_i = - \frac{\partial \Phi}{\partial x_i} + \varepsilon_{ijk} \frac{\partial A_k}{\partial x_j} \; . \tag{2-9}$$

In Equation (2-9), ε_{ijk} is the alternating tensor. The scalar potential is introduced to facilitate setting the boundary conditions on the velocity components. Hirasaki and Hellums, Reference 7, have shown that a unique vector potential A_i, within the gradient of an arbitrary harmonic function, exists such that

$$\frac{\partial A_i}{\partial x_i} = 0. \tag{2-10}$$

By taking the divergence of Equation (2-9) and introducing the conditions imposed by Equation (2-1) (the conservation of mass) and Equation (2-10), a partial differential equation for the scalar potential follows,

$$\frac{\partial^2 \Phi}{\partial x_i \partial x_i} = 0. \tag{2-11}$$

A differential equation for the vector potential is derived by taking the curl of Equation (2-9) and using Equation (2-10), which gives

$$\frac{\partial^2 A_i}{\partial x_j \partial x_j} = - \Omega_i, \tag{2-12}$$

where the vorticity is defined by

$$\Omega_i = \varepsilon_{ijk} \frac{\partial u_k}{\partial x_j}. \tag{2-13}$$

Consider next the equation for the conservation of momentum. Taking the curl of Equation (2-2) and utilizing Equation (2-13) eliminates the pressure from the momentum equation and results in a transport equation for the vorticity. The pressure is then computed from a Poisson equation, which is derived by

taking the divergence of Equation (2-2).

Carrying out the steps outlined in the previous paragraph, introducing a characteristic length D and characteristic velocity V_0 to normalize the equations, and expanding the equations in the cartesian coordinates (x, y, z) with velocity components (u, v, w) results in the system of dimensionless equations given below.

Poisson equation for the scalar potential:

$$\frac{\partial^2 \Phi}{\partial x^2} + \frac{\partial^2 \Phi}{\partial y^2} + \frac{\partial^2 \Phi}{\partial z^2} = 0 \qquad (2\text{-}14)$$

Poisson equation for the x component of vector potential:

$$\frac{\partial^2 A_x}{\partial x^2} + \frac{\partial^2 A_x}{\partial y^2} + \frac{\partial^2 A_x}{\partial z^2} = -\Omega_x \qquad (2\text{-}15)$$

Poisson equation for the y component of vector potential:

$$\frac{\partial^2 A_y}{\partial x^2} + \frac{\partial^2 A_y}{\partial y^2} + \frac{\partial^2 A_y}{\partial z^2} = -\Omega_y \qquad (2\text{-}16)$$

Poisson equation for the z component of vector potential:

$$\frac{\partial^2 A_z}{\partial x^2} + \frac{\partial^2 A_z}{\partial y^2} + \frac{\partial^2 A_z}{\partial z^2} = -\Omega_z \qquad (2\text{-}17)$$

Transport equation for the x component of vorticity:

$$[1 + \varepsilon(\bar{r})]\left(\frac{\partial^2\Omega_x}{\partial x^2} + \frac{\partial^2\Omega_x}{\partial y^2} + \frac{\partial^2\Omega_x}{\partial z^2}\right) + Re\left[\frac{1}{Re}\frac{\partial\varepsilon(\bar{r})}{\partial x} - u\right]\frac{\partial\Omega_x}{\partial x} + Re\left[\frac{1}{Re}\frac{\partial\varepsilon(\bar{r})}{\partial y} - v\right]$$

$$\times \frac{\partial\Omega_x}{\partial y} + Re\left[\frac{1}{Re}\frac{\partial\varepsilon(\bar{r})}{\partial z} - w\right]\frac{\partial\Omega_x}{\partial z} = Re\left[\left(\frac{\partial v}{\partial y} + \frac{\partial w}{\partial z}\right)\Omega_x + \frac{\partial u}{\partial y}\frac{\partial w}{\partial x} - \frac{\partial u}{\partial z}\frac{\partial v}{\partial x}\right]$$

$$+ \left[-\frac{\partial^2\varepsilon(\bar{r})}{\partial x\partial y}\left(\frac{\partial w}{\partial x} + \frac{\partial u}{\partial z}\right) - 2\frac{\partial^2\varepsilon(\bar{r})}{\partial y\partial z}\left(\frac{\partial w}{\partial z} - \frac{\partial v}{\partial y}\right) - \frac{\partial^2\varepsilon(\bar{r})}{\partial y^2}\left(\frac{\partial w}{\partial y} + \frac{\partial v}{\partial z}\right)\right.$$

$$- \frac{\partial\varepsilon(\bar{r})}{\partial y}\left(\frac{\partial^2 w}{\partial x^2} + \frac{\partial^2 w}{\partial y^2} + \frac{\partial^2 w}{\partial z^2}\right) + \frac{\partial\varepsilon(\bar{r})}{\partial z}\left(\frac{\partial^2 v}{\partial x^2} + \frac{\partial^2 v}{\partial y^2} + \frac{\partial^2 v}{\partial z^2}\right)$$

$$\left. + \frac{\partial^2\varepsilon(\bar{r})}{\partial x\partial z}\left(\frac{\partial v}{\partial x} + \frac{\partial u}{\partial y}\right) + \frac{\partial^2\varepsilon(\bar{r})}{\partial z^2}\left(\frac{\partial w}{\partial y} + \frac{\partial v}{\partial z}\right)\right] \qquad (2\text{-}18)$$

Transport equation for the y component of vorticity:

$$[1 + \varepsilon(\bar{r})]\left(\frac{\partial^2\Omega_y}{\partial x^2} + \frac{\partial^2\Omega_y}{\partial y^2} + \frac{\partial^2\Omega_y}{\partial z^2}\right) + Re\left[\frac{1}{Re}\frac{\partial\varepsilon(\bar{r})}{\partial x} - u\right]\frac{\partial\Omega_y}{\partial x}$$

$$+ Re\left[\frac{1}{Re}\frac{\partial\varepsilon(\bar{r})}{\partial y} - v\right]\frac{\partial\Omega_y}{\partial y} + Re\left[\frac{1}{Re}\frac{\partial\varepsilon(\bar{r})}{\partial z} - w\right]\frac{\partial\Omega_y}{\partial z}$$

$$= Re\left[\left(\frac{\partial u}{\partial x} + \frac{\partial w}{\partial z}\right)\Omega_y + \frac{\partial v}{\partial z}\frac{\partial u}{\partial y} - \frac{\partial v}{\partial x}\frac{\partial w}{\partial y}\right] + \left[\frac{\partial^2\varepsilon(\bar{r})}{\partial x\partial y}\left(\frac{\partial w}{\partial y} + \frac{\partial v}{\partial z}\right)\right.$$

$$- \frac{\partial^2\varepsilon(\bar{r})}{\partial y\partial z}\left(\frac{\partial v}{\partial x} + \frac{\partial u}{\partial y}\right) + \frac{\partial^2\varepsilon(\bar{r})}{\partial x^2}\left(\frac{\partial w}{\partial x} + \frac{\partial u}{\partial z}\right) + \frac{\partial\varepsilon(\bar{r})}{\partial x}\left(\frac{\partial^2 w}{\partial x^2} + \frac{\partial^2 w}{\partial y^2}\right.$$

$$\left.\left. + \frac{\partial^2 w}{\partial z^2}\right) - \frac{\partial\varepsilon(\bar{r})}{\partial z}\left(\frac{\partial^2 u}{\partial x^2} + \frac{\partial^2 u}{\partial y^2} + \frac{\partial^2 u}{\partial z^2}\right) - 2\frac{\partial^2\varepsilon(\bar{r})}{\partial x\partial z}\left(\frac{\partial u}{\partial x} - \frac{\partial w}{\partial z}\right)\right.$$

$$- \frac{\partial^2 \varepsilon(\bar{r})}{\partial z^2} \left(\frac{\partial w}{\partial x} + \frac{\partial u}{\partial z} \right) \Bigg] \tag{2-19}$$

Transport equation for the z component of vorticity:

$$[1 + \varepsilon(\bar{r})] \left(\frac{\partial^2 \Omega_z}{\partial x^2} + \frac{\partial^2 \Omega_z}{\partial y^2} + \frac{\partial^2 \Omega_z}{\partial z^2} \right) + \mathrm{Re} \left[\frac{1}{\mathrm{Re}} \frac{\partial \varepsilon(\bar{r})}{\partial x} - u \right] \frac{\partial \Omega_z}{\partial x}$$

$$+ \mathrm{Re} \left[\frac{1}{\mathrm{Re}} \frac{\partial \varepsilon(\bar{r})}{\partial y} - v \right] \frac{\partial \Omega_z}{\partial y} + \mathrm{Re} \left[\frac{1}{\mathrm{Re}} \frac{\partial \varepsilon(\bar{r})}{\partial z} - w \right] \frac{\partial \Omega_z}{\partial z} = \mathrm{Re} \left[\left(\frac{\partial u}{\partial x} \right.\right.$$

$$\left.\left. + \frac{\partial v}{\partial y} \right) \Omega_z + \frac{\partial w}{\partial x} \frac{\partial v}{\partial z} - \frac{\partial w}{\partial y} \frac{\partial u}{\partial z} \right] + \left[- \frac{\partial^2 \varepsilon(\bar{r})}{\partial x^2} \left(\frac{\partial v}{\partial x} + \frac{\partial u}{\partial y} \right) \right.$$

$$- \frac{\partial \varepsilon(\bar{r})}{\partial x} \left(\frac{\partial^2 v}{\partial x^2} + \frac{\partial^2 v}{\partial y^2} + \frac{\partial^2 v}{\partial z^2} \right) - 2 \frac{\partial^2 \varepsilon(\bar{r})}{\partial x \partial y} \left(\frac{\partial v}{\partial y} - \frac{\partial u}{\partial x} \right) + \frac{\partial \varepsilon(\bar{r})}{\partial y} \left(\frac{\partial^2 u}{\partial x^2} \right.$$

$$\left. + \frac{\partial^2 u}{\partial y^2} + \frac{\partial^2 u}{\partial z^2} \right) - \frac{\partial \varepsilon^2(\bar{r})}{\partial x \partial z} \left(\frac{\partial w}{\partial y} + \frac{\partial v}{\partial z} \right) + \frac{\partial^2 \varepsilon(\bar{r})}{\partial y^2} \left(\frac{\partial v}{\partial x} + \frac{\partial u}{\partial y} \right)$$

$$\left. + \frac{\partial^2 \varepsilon(\bar{r})}{\partial y \partial z} \left(\frac{\partial w}{\partial x} + \frac{\partial u}{\partial z} \right) \right] \tag{2-20}$$

Transport equation for the turbulent kinetic energy:

$$[1 + \varepsilon(\lambda \bar{r})] \left(\frac{\partial^2 k}{\partial x^2} + \frac{\partial^2 k}{\partial y^2} + \frac{\partial^2 k}{\partial z^2} \right) + \mathrm{Re} \left[\frac{1}{\mathrm{Re}} \frac{\partial \varepsilon(\lambda \bar{r})}{\partial x} - u \right] \frac{\partial k}{\partial x}$$

$$+ \mathrm{Re} \left[\frac{1}{\mathrm{Re}} \frac{\partial \varepsilon(\lambda \bar{r})}{\partial y} - v \right] \frac{\partial k}{\partial y} + \mathrm{Re} \left[\frac{1}{\mathrm{Re}} \frac{\partial \varepsilon(\lambda \bar{r})}{\partial z} - w \right] \frac{\partial k}{\partial z}$$

$$= \frac{Ck[1 + \varepsilon(\lambda \bar{r})]}{L^2} - \varepsilon(\bar{r}) \left[2 \frac{\partial u}{\partial x} \frac{\partial u}{\partial x} + \left(\frac{\partial v}{\partial x} + \frac{\partial u}{\partial y} \right) \frac{\partial u}{\partial y} \right.$$

$$+\left(\frac{\partial w}{\partial x}+\frac{\partial u}{\partial z}\right)\frac{\partial u}{\partial z}+\left(\frac{\partial v}{\partial x}+\frac{\partial u}{\partial y}\right)\frac{\partial v}{\partial x}+2\,\frac{\partial v}{\partial y}\,\frac{\partial v}{\partial y}+\left(\frac{\partial w}{\partial y}+\frac{\partial v}{\partial z}\right)\frac{\partial v}{\partial z}$$

$$+\left(\frac{\partial w}{\partial x}+\frac{\partial u}{\partial z}\right)\frac{\partial w}{\partial x}+\left(\frac{\partial w}{\partial y}+\frac{\partial v}{\partial z}\right)\frac{\partial w}{\partial y}+2\,\frac{\partial w}{\partial z}\,\frac{\partial w}{\partial z}\Bigg] \qquad (2\text{-}21)$$

Poisson equation for the static pressure:

$$\frac{\partial^2 p}{\partial x^2}+\frac{\partial^2 p}{\partial y^2}+\frac{\partial^2 p}{\partial z^2}=\frac{4}{Re}\Bigg[\frac{\partial^2\varepsilon(\bar{r})}{\partial x^2}\frac{\partial u}{\partial x}+\frac{\partial^2\varepsilon(\bar{r})}{\partial y^2}\frac{\partial v}{\partial y}+\frac{\partial^2\varepsilon(\bar{r})}{\partial z^2}\frac{\partial w}{\partial z}+\frac{\partial\varepsilon(\bar{r})}{\partial x}\left(\frac{\partial^2 u}{\partial x^2}\right.$$

$$\left.+\frac{\partial^2 u}{\partial y^2}+\frac{\partial^2 u}{\partial z^2}\right)+\frac{\partial\varepsilon(\bar{r})}{\partial y}\left(\frac{\partial^2 v}{\partial x^2}+\frac{\partial^2 v}{\partial y^2}+\frac{\partial^2 v}{\partial z^2}\right)+\frac{\partial\varepsilon(\bar{r})}{\partial z}\left(\frac{\partial^2 w}{\partial x^2}+\frac{\partial^2 w}{\partial y^2}+\frac{\partial^2 w}{\partial z^2}\right)$$

$$+\frac{\partial^2\varepsilon(\bar{r})}{\partial x\partial y}\left(\frac{\partial u}{\partial y}+\frac{\partial v}{\partial x}\right)+\frac{\partial^2\varepsilon(\bar{r})}{\partial x\partial z}\left(\frac{\partial u}{\partial z}+\frac{\partial w}{\partial x}\right)+\frac{\partial^2\varepsilon(\bar{r})}{\partial y\partial z}\left(\frac{\partial v}{\partial z}+\frac{\partial w}{\partial y}\right)\Bigg]$$

$$-\frac{4}{3}\left(\frac{\partial^2 k}{\partial x^2}+\frac{\partial^2 k}{\partial y^2}+\frac{\partial^2 k}{\partial z^2}\right)-2\left(\frac{\partial u}{\partial x}\frac{\partial u}{\partial x}+\frac{\partial v}{\partial x}\frac{\partial u}{\partial y}+\frac{\partial w}{\partial x}\frac{\partial u}{\partial z}+\frac{\partial u}{\partial y}\frac{\partial v}{\partial x}\right.$$

$$\left.+\frac{\partial v}{\partial y}\frac{\partial v}{\partial y}+\frac{\partial w}{\partial y}\frac{\partial v}{\partial z}+\frac{\partial u}{\partial z}\frac{\partial w}{\partial x}+\frac{\partial v}{\partial z}\frac{\partial w}{\partial y}+\frac{\partial w}{\partial z}\frac{\partial w}{\partial z}\right) \qquad (2\text{-}22)$$

The only dimensionless parameter which enters the system of equations is the Reynolds number, $Re = V_o D/\nu$. The location in the flowfield where V_o and D are chosen will be defined subsequently for the particular configurations of interest. The Poisson equation for the scalar potential is independent of Reynolds number and need be solved only once for a given geometry and set of boundary conditions.

2.2 The Boundary Conditions

In the system of equations presented in Section 2.1, there are nine elliptic partial-differential equations which must be solved for the following nine flow properties: Φ, A_x, A_y, A_z, Ω_x, Ω_y, Ω_z, k, and p.

The velocity components normal to the surface S of the computational domain with volume R are assumed to be known and are used to evaluate the normal derivatives of the scalar potential on the boundaries:

$$\frac{\partial \Phi}{\partial n} = - n_i u_i, \tag{2-23}$$

where n_i denotes a unit vector normal to the boundary. Equation (2-23) provides the necessary boundary conditions with which to solve Equation (2-14) for Φ within an arbitrary constant. Since only the gradients of the scalar potential are required to compute the velocity components, the value of the constant is immaterial.

The boundary conditions on the vector potential A_i are chosen such that the normal component is determined by the solenoidal condition, Equation (2-10), and the tangential components are taken to be zero. For a flat surface, these boundary conditions are

$$\frac{\partial A_n}{\partial n} = 0, \quad A_t = 0, \tag{2-24}$$

where t denotes the tangential component. Since the Poisson equations for the components of the vector potential are dependent on the vorticity, which appears as a source term on the right side of Equation (2-12), they cannot be solved independently as can the Poisson equation for scalar potential. Rather, the vector potential equations in combination with the remaining equations must be solved iteratively for A on the boundaries as well as in the interior region of the computational domain.

Similarly, the vorticity on the boundaries must be computed iteratively. At each cycle in the iteration, the velocity components at the boundaries are updated from Equation (2-9),

$$u_i = -\frac{\partial \Phi}{\partial x_i} + \varepsilon_{ijk} \frac{\partial A_k}{\partial x_j}, \tag{2-9}$$

using the fixed value of Φ and the current value of A_k. In turn, with u_i updated on the boundaries, the boundary values of the vorticity are recomputed from Equation (2-13),

$$\Omega_i = \varepsilon_{ijk} \frac{\partial u_k}{\partial x_j}, \tag{2-13}$$

and used during the next iterative cycle in the solution of the vorticity transport equations. The turbulent kinetic energy variation is related to the magnitude of the vorticity on the boundaries through a simple mixing-length formulation, except on a solid surface where k = 0, and therefore is also computed iteratively during the course of the calculations.

The solution of the Poisson equation for the static pressure can be deferred until a convergent solution is obtained for A_x, A_y, A_z, Ω_x, Ω_y, Ω_z, and k. The boundary conditions required for Equation (2-22) follow from the pressure gradients given by the component momentum equations.

$$\frac{\partial p}{\partial x} = \frac{2}{Re}\left[2\frac{\partial \varepsilon(\bar{r})}{\partial x}\frac{\partial u}{\partial x} + \frac{\partial \varepsilon(\bar{r})}{\partial y}\left(\frac{\partial u}{\partial y} + \frac{\partial v}{\partial x}\right) + \frac{\partial \varepsilon(\bar{r})}{\partial z}\left(\frac{\partial u}{\partial z} + \frac{\partial w}{\partial x}\right)\right.$$
$$\left. + [1 + \varepsilon(\bar{r})]\left(\frac{\partial^2 u}{\partial x^2} + \frac{\partial^2 u}{\partial y^2} + \frac{\partial^2 u}{\partial z^2}\right)\right] - \frac{4}{3}\frac{\partial k}{\partial x} - 2\left(u\frac{\partial u}{\partial x} + v\frac{\partial u}{\partial y} + w\frac{\partial u}{\partial z}\right) \tag{2-25}$$

$$\frac{\partial p}{\partial y} = \frac{2}{Re}\left[\frac{\partial \varepsilon(\bar{r})}{\partial x}\left(\frac{\partial v}{\partial x} + \frac{\partial u}{\partial y}\right) + 2\,\frac{\partial \varepsilon(\bar{r})}{\partial y}\,\frac{\partial v}{\partial y} + \frac{\partial \varepsilon(\bar{r})}{\partial z}\left(\frac{\partial v}{\partial z} + \frac{\partial w}{\partial y}\right)\right.$$

$$\left. + [1 + \varepsilon(\bar{r})]\left(\frac{\partial^2 v}{\partial x^2} + \frac{\partial^2 v}{\partial y^2} + \frac{\partial^2 v}{\partial z^2}\right)\right] - \frac{4}{3}\frac{\partial k}{\partial y} - 2\left(u\,\frac{\partial v}{\partial x} + v\,\frac{\partial v}{\partial y} + w\,\frac{\partial v}{\partial z}\right) \tag{2-26}$$

$$\frac{\partial p}{\partial z} = \frac{2}{Re}\left[\frac{\partial \varepsilon(\bar{r})}{\partial x}\left(\frac{\partial w}{\partial x} + \frac{\partial u}{\partial z}\right) + \frac{\partial \varepsilon(\bar{r})}{\partial y}\left(\frac{\partial w}{\partial y} + \frac{\partial v}{\partial z}\right) + 2\,\frac{\partial \varepsilon(\bar{r})}{\partial z}\,\frac{\partial w}{\partial z}\right.$$

$$\left. + [1 + \varepsilon(\bar{r})]\left(\frac{\partial^2 w}{\partial x^2} + \frac{\partial^2 w}{\partial y^2} + \frac{\partial^2 w}{\partial z^2}\right)\right] - \frac{4}{3}\frac{\partial k}{\partial z} - 2\left(u\,\frac{\partial w}{\partial x} + v\,\frac{\partial w}{\partial y} + w\,\frac{\partial w}{\partial z}\right) \tag{2-27}$$

The right sides of Equations (2-25) through (2-27) are known from the solution of the equations for the scalar potential, vector potential, vorticity, and turbulent kinetic energy.

The two computational domains that are used in the present work and for which the normal velocity components at the surface must be specified are shown in Figure 2, where all dimensions have been normalized by D. For the case of two equal- or unequal-strength jets with normal impingement, Figure 2(a), the boundaries $z = 0$, $x = 0$, and $z = S$ are jet symmetry planes. The boundary $y = 0$ is the ground plane, the boundary $y = h$ is the inflow plane through which the primary jets enter the computational domain, and the boundary $x = w$ is the outflow plane through which the wall jet exits the computational domain. For the case of two equal- or unequal-strength jets with inclined impingement, Figure 2(b), there is only one symmetry plane, $x = 0$. The boundary $y = 0$ is the ground plane, the boundary $y = h$ is the inflow plane, and the boundaries $z = 0$, $x = w$, and $z = L$ are outflow planes.

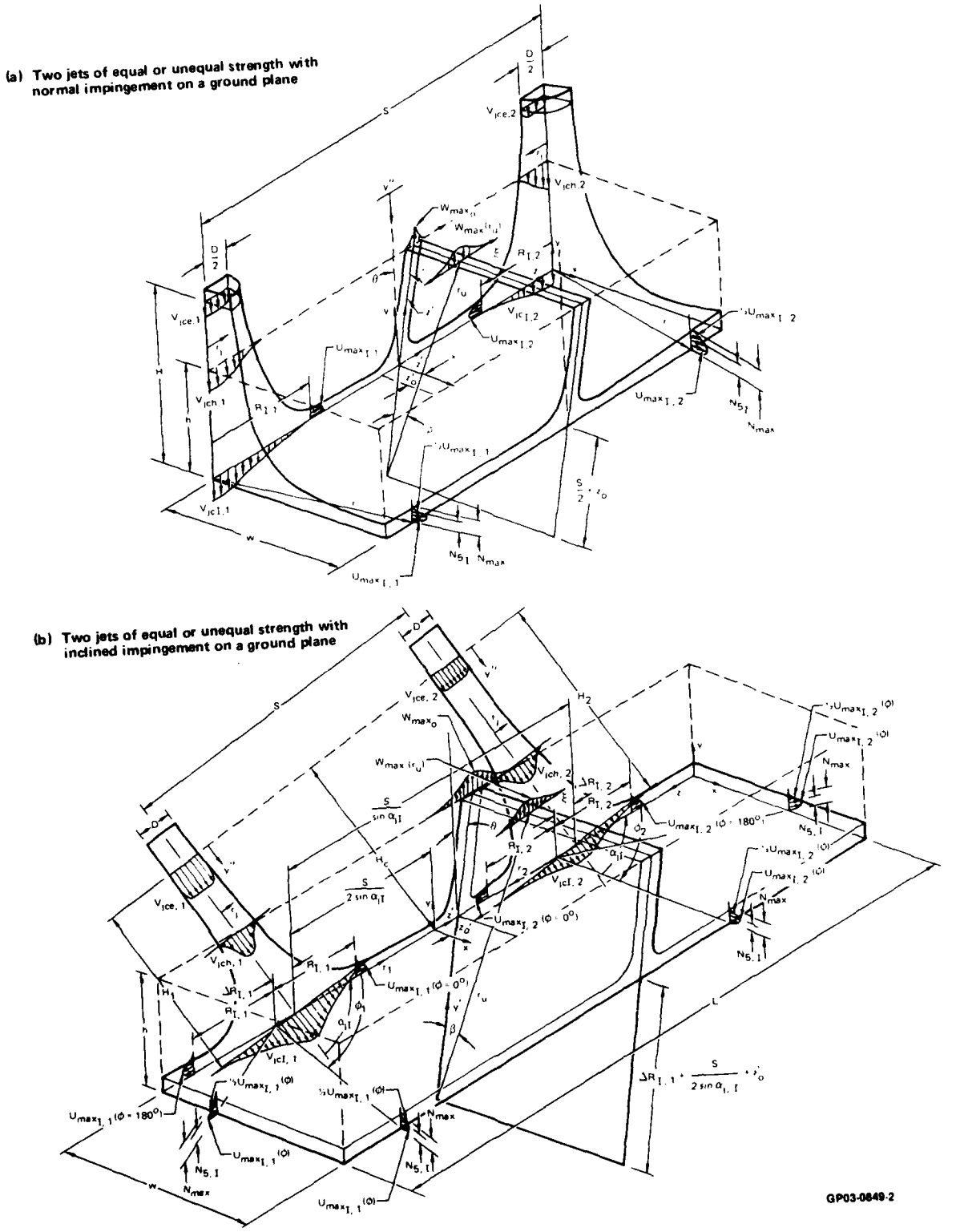

Figure 2. Definition of the computational regions for the jet-impingement configurations.

The manner in which the required velocity profiles through the primary jets, the wall jet, and the fountain are computed at the boundaries of the computational domain is presented in Appendix A for the most general case of interest, unequal-strength jets with inclined impingement. For dual jets with normal impingement, the simplification that can be introduced in the analysis is noted.

In the specification of the boundary conditions, it is necessary that the imposed inflow and outflow velocity profiles satisfy the global conservation of mass for the computational domain. The Poisson equation for the scalar potential, Equation (2-11), has a solution if and only if

$$\int_R \frac{\partial^2 \Phi}{\partial x_i \partial x_i} \, dV = \int_S \frac{\partial \Phi}{\partial x_i} \, n_i dS' = \int_S \frac{\partial \Phi}{\partial n} \, dS' = - \int_S u_i n_i dS' = 0. \qquad (2\text{-}28)$$

If the net mass flux $\int_S u_i n_i dS'$ is not extremely small (typically on the order of 10^{-6}), a convergent solution of Equation (2-11) cannot be obtained. In the present work, the normal velocity components required in the analysis are specified such that the trapezoidal approximation to Equation (2-28) is satisfied within the required tolerance.

The finite-difference technique that is used to solve the coupled system of nonlinear elliptic equations is described in the next section.

3. THE NUMERICAL SOLUTION SCHEME

This section is a discussion of the finite-difference techniques used to solve the partial differential equations which describe the flowfield. The Poisson-type equations are discretized using the standard central-difference algorithm, and the transport-type equations are discretized using an augmented-central-difference algorithm. The manner in which the coupled system of equations is iteratively solved and the convergence characteristics of the solution are described.

3.1 The Discretization of the Poisson-Type Equations

The Poisson equations for the scalar potential, the three components of the vector potential, and the pressure can all be written in the following form in terms of an arbitrary flow variable ϕ and source term σ:

$$\frac{\partial^2 \phi}{\partial x^2} + \frac{\partial^2 \phi}{\partial y^2} + \frac{\partial^2 \phi}{\partial z^2} = \sigma. \tag{3-1}$$

Writing Equation (3-1) for the scalar potential, ϕ is replaced with Φ, and σ is 0, which reduces the equation to Laplace form. The boundary conditions are fully Neumann,

$$\frac{\partial \Phi}{\partial n} = - n_i u_i. \tag{3-2}$$

Writing Equation (3-2) for the components of the vector potential, ϕ is replaced with A_x, A_y, and A_z for σ given by $- \Omega_x$, $- \Omega_y$, and $- \Omega_z$, respectively. The boundary conditions are mixed Neumann and Dirichlet,

$$\frac{\partial A_n}{\partial n} = 0; \quad A_i = 0, \quad i \neq n. \tag{3-3}$$

Writing Equation (3-1) for the static pressure, ϕ is replaced with p and σ is given by the right side of Equation (2-22), which is denoted σ_p for simplicity. The boundary conditions are Neumann,

$$\frac{\partial p}{\partial n} = \sigma_n, \tag{3-4}$$

where the pressure gradient normal to the surface is given by either Equation (2-25), (2-26), or (2-27). However, in the solution of Equation (3-3) for p, the pressure is integrated along the plane x = 0 of the computational domain in order to set the level, which replaces one of the Neumann conditions by a Dirichlet condition.

To write Equation (3-1) in finite-difference form, the three-dimensional nodal network shown in Figure 3 is introduced. A uniform grid spacing h is used in each of the coordinate directions, so that x = h(i - 1), y = h(j - 1), and z = h(k - 1), where i, j, and k are the respective node indices. The conventional central-difference algorithm is introduced for which the second derivatives centered at an interior point in the nodal network are given by

$$\left.\frac{\partial^2 \phi}{\partial x^2}\right|_{i,j,k} = \frac{\phi_{i+1,j,k} - 2\phi_{i,j,k} + \phi_{i-1,j,k}}{h^2} \tag{3-5}$$

$$\left.\frac{\partial^2 \phi}{\partial y^2}\right|_{i,j,k} = \frac{\phi_{i,j+1,k} - 2\phi_{i,j,k} + \phi_{i,j-1,k}}{h^2} \tag{3-6}$$

$$\left.\frac{\partial^2 \phi}{\partial z^2}\right|_{i,j,k} = \frac{\phi_{i,j,k+1} - 2\phi_{i,j,k} + \phi_{i,j,k-1}}{h^2} . \tag{3-7}$$

When Equations (3-5) through (3-7) are substituted into Equation (3-1), the discretized form of the Poisson equation is

$$\phi_{i+1,j,k} + \phi_{i-1,j,k} + \phi_{i,j+1,k} + \phi_{i,j-1,k} + \phi_{i,j,k+1}$$

$$+ \phi_{i,j,k-1} - 6\phi_{i,j,k} = h^2\sigma_{i,j,k} \quad . \tag{3-8}$$

Equation (3-8) applies directly to the interior of the computational domain: $1 < i < I$, $1 < j < J$, and $1 < k < K$, where I, J, and K denote the maximum values of the respective node indices.

The manner in which the boundary conditions are imposed on Equation (3-8) depends on whether they are Dirichlet or Neumann. In the former case, if a value of ϕ on the left side of Equation (3-8) is known, it is transferred to the right side of the equation and is eliminated as an element of the solution vector. In the case of a Neumann boundary condition, Equation (3-8) is applied at the boundary to solve for ϕ at that location. The value of ϕ on the line outside the computational domain is computed by treating this line as an image of the line adjacent to the boundary on the inside of the computational domain. The image-line value of ϕ is related to the interior-line value through the central-difference discretization of the Neumann

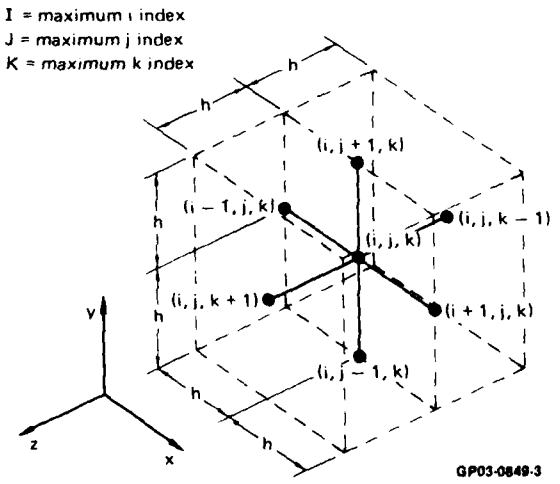

Figure 3. The three-dimensional finite-difference stencil.

boundary condition. Consider, for example, the case where $\left.\frac{\partial \phi}{\partial x}\right|_{I,j,k}$ is known at the boundary x = h(I-1). The finite-difference form of this derivative is given by

$$\left.\frac{\partial \phi}{\partial x}\right|_{I,j,k} = \frac{\phi_{I+1,j,k} - \phi_{I-1,j,k}}{2h} , \tag{3-9}$$

from which it follows that

$$\phi_{I+1,j,k} = \phi_{I-1,j,k} + 2h \left.\frac{\partial \phi}{\partial x}\right|_{I,j,k} . \tag{3-10}$$

Equation (3-10) is then substituted into Equation (3-8) written for i = I. Neumann conditions on the other boundaries are treated in an analogous fashion.

The entire system of algebraic finite-difference equations can be written in the following matrix form:

$$\tilde{A}\,\bar{\phi} = \bar{b} , \tag{3-11}$$

where

$$\tilde{A} = [A_1, A_2, \ldots, A_k] , \tag{3-12}$$

$$\phi = (\phi_{i,j,k}) , \tag{3-13}$$

and A_k is a block tridiagonal matrix with diagonal elements

$$\begin{bmatrix} -6 & 2 & 0 & 0 & 0 & \cdots & 0 \\ 1 & -6 & 1 & 0 & 0 & \cdots & 0 \\ 0 & 1 & -6 & 1 & 0 & \cdots & 0 \\ 0 & 0 & \ddots & \ddots & \ddots & \ddots & 0 \\ \vdots & \vdots & \ddots & 0 & 1 & -6 & 1 \\ 0 & 0 & \cdots & 0 & 0 & 2 & -6 \end{bmatrix} .$$

The superdiagonal and subdiagonal elements are all (δ_{ij}), except the first superdiagonal element and the last subdiagonal element, which are $(2\delta_{ij})$.

In Equation (3-12), A_k represents a coefficient matrix for a fixed k plane. The terms $\phi_{i,j,k+1}$ and $\phi_{i,j,k-1}$ have been transferred to the right side of Equation (3-8). Gauss-Seidel line relaxation is used to solve Equation (3-11), which requires an additional transfer of terms to the right side of Equation (3-8). For example, when j is allowed to vary in a fixed k plane, the terms $\phi_{i+1,j,k}$ and $\phi_{i-1,j,k}$ are included in the right-side vector. Specifically, the altered form of $\bar{b}$ becomes

$$\hat{b}_{ik} = \left(h^2\sigma_{i,j,k} - \phi_{i-1,j,k} - \phi_{i+1,j,k} - \phi_{i,j,k+1} - \phi_{i,j,k-1} + 2h\delta_{1,j}\left.\frac{\partial\phi}{\partial y}\right|_{i,j,k} - 2h\delta_{J,j}\left.\frac{\partial\phi}{\partial y}\right|_{i,j,k}\right)_{j=1}^{J} . \qquad (3\text{-}15)$$

Elements from the superdiagonal and subdiagonal of A_k are included in $\hat{b}_{ik}$. Further details about the solution of the Poisson-type equations in conjunction with the solution of the transport-type equations are given in Section 3.3.

3.2 The Discretization of the Transport-Type Equations

The transport equations for the three components of the vorticity and the turbulent kinetic energy can be written in the following form, where again ϕ is an arbitrary flow variable and σ_1 and σ_2 are source terms:

$$\alpha\left(\frac{\partial^2\phi}{\partial x^2} + \frac{\partial^2\phi}{\partial y^2} + \frac{\partial^2\phi}{\partial z^2}\right) + Re\,\beta\frac{\partial\phi}{\partial x} + Re\gamma\frac{\partial\phi}{\partial y} + Re\delta\frac{\partial\phi}{\partial z} = Re\sigma_1 + \sigma_2 . \qquad (3\text{-}16)$$

Writing Equation (3-16) for the components of the vorticity, ϕ is replaced with Ω_x, Ω_y, and Ω_z. The definitions of the coefficients α, β, γ, and δ and

the source terms σ_1 and σ_2 follow directly from an inspection of Equations (2-18) to (2-20). The boundary conditions are fully Dirichlet,

$$\Omega_i = \sigma_\omega \ . \tag{3-17}$$

Writing Equation (3-16) for the turbulent kinetic energy, ϕ is replaced with k; α, β, γ, δ, σ_1, and σ_2 follow from Equation (2-21). The boundary conditions are mixed Neumann and Dirichlet,

$$\frac{\partial k}{\partial n} = 0, \ k = \sigma_k \ . \tag{3-18}$$

Equation (3-16) cannot be solved for an arbitrary Reynolds number using the conventional central-difference approximations to the derivatives. The reason for this difficulty is that the transport-type equations contain the Reynolds number as a coefficient of each convective term. Consequently, with the standard central-difference alogrithm, the discretized system of equations is diagonally dominant for only a limited range in Reynolds number. Diagonal dominance is necessary to obtain convergence in the iterative solution of the discretized system of equations.

To ensure convergence for all Reynolds numbers, the second-order-accurate augmented-central-difference (ACD) algorithm developed by Hoffman, Reference 8, was extended to the three-dimensional transport equation represented by Equation (3-16). The basis of this method can be illustrated by considering the derivative $\partial\phi/\partial x$ of the latter equation. At an interior point i,j,k in the nodal network, this term is evaluated in terms of the adjacent points in the x direction with the following truncated Taylor-series representation and standard central-difference approximation to the first derivative:

$$\left.\frac{\partial \phi}{\partial x}\right|_{i,j,k} = \frac{\phi_{i+1,j,k} - \phi_{i-1,j,k}}{2h} - \left.\frac{h^2}{6}\frac{\partial^3 \phi}{\partial x^3}\right|_{i,j,k} - \left.\frac{h^4}{5!}\frac{\partial^5 \phi}{\partial x^5}\right|_{i,j,k} \tag{3-19}$$

In the ACD scheme, the derivative $\partial^3\phi/\partial x^3$ is retained and expressed in terms of lower-order derivatives by differentiating Equation (3-16) with respect to x. The result is

$$\left.\frac{\partial\phi}{\partial x}\right|_{i,j,k} = \frac{\phi_{i+1,j,k} - \phi_{i-1,j,k}}{2h} + \frac{h^2}{6}\,\mathrm{Re}\,\frac{\beta}{\alpha}\left.\frac{\partial^2\phi}{\partial x^2}\right|_{i,j,k}$$

$$+ \frac{h^2}{6}\,\mathrm{Re}\,S_{1i,j,k} + 0\,(\mathrm{Reh}^2)\,, \tag{3-20}$$

where

$$S_{1i,j,k} = \left(\frac{1}{\alpha}\frac{\partial\beta}{\partial x}\frac{\partial\phi}{\partial x} + \frac{1}{\alpha}\frac{\partial\gamma}{\partial x}\frac{\partial\phi}{\partial y} + \frac{1}{\alpha}\gamma\frac{\partial^2\phi}{\partial x\partial y}\right.$$

$$\left. + \frac{1}{\alpha}\frac{\partial\delta}{\partial x}\frac{\partial\phi}{\partial z} + \frac{1}{\alpha}\delta\frac{\partial^2\phi}{\partial x\partial z} - \frac{1}{\alpha}\frac{\partial\sigma_1}{\partial x}\right)\Bigg|_{i,j,k}. \tag{3-21}$$

The derivatives $\partial\phi/\partial y$ and $\partial\phi/\partial z$ in Equation (3-16) are represented in an analogous fashion with the ACD algorithm. The following is the discretized form of the transport-type equation:

$$C_{1i,j,k}\,\phi_{i+1,j,k} + C_{2i,j,k}\,\phi_{i-1,j,k} + C_{3i,j,k}\,\phi_{i,j+1,k}$$

$$+ C_{4i,j,k}\,\phi_{i,j-1,k} + C_{5i,j,k}\,\phi_{i,j,k+1} + C_{6i,j,k}\,\phi_{i,j,k-1}$$

$$- C_{7i,j,k}\,\phi_{i,j,k} = D_{i,j,k} \tag{3-22}$$

The definitions of the coefficients are given below.

$$C_{1i,j,k} = \frac{1}{h^2}\left(\alpha + \frac{Re\beta h}{2} + \frac{Re^2h^2}{6}\frac{\beta^2}{\alpha}\right)\Bigg|_{i,j,k} \tag{3-23}$$

$$C_{2i,j,k} = \frac{1}{h^2}\left(\alpha - \frac{Re\beta h}{2} + \frac{Re^2h^2}{6}\frac{\beta^2}{\alpha}\right)\Bigg|_{i,j,k} \tag{3-24}$$

$$C_{3i,j,k} = \frac{1}{h^2}\left(\alpha + \frac{Re\gamma h}{2} + \frac{Re^2h^2}{6}\frac{\gamma^2}{\alpha}\right)\Bigg|_{i,j,k} \tag{3-25}$$

$$C_{4i,j,k} = \frac{1}{h^2}\left(\alpha - \frac{Re\gamma h}{2} + \frac{Re^2h^2}{6}\frac{\gamma^2}{\alpha}\right)\Bigg|_{i,j,k} \tag{3-26}$$

$$C_{5i,j,k} = \frac{1}{h^2}\left(\alpha + \frac{Re\delta h}{2} + \frac{Re^2h^2}{6}\frac{\delta^2}{\alpha}\right)\Bigg|_{i,j,k} \tag{3-27}$$

$$C_{6i,j,k} = \frac{1}{h^2}\left(\alpha - \frac{Re\delta h}{2} + \frac{Re^2h^2}{6}\frac{\delta^2}{\alpha}\right)\Bigg|_{i,j,k} \tag{3-28}$$

$$C_{7i,j,k} = \frac{2}{h^2}\left(3\alpha + \frac{Re^2h^2}{6}\frac{\beta^2}{\alpha} + \frac{Re^2h^2}{6}\frac{\gamma^2}{\alpha} + \frac{Re^2h^2}{6}\frac{\delta^2}{\alpha}\right)\Bigg|_{i,j,k} \tag{3-29}$$

$$D_{i,j,k} = Re\sigma_{1i,j,k} + \sigma_{2i,j,k} - \frac{Re^2h^2}{6}\left(\beta S_1 + \gamma S_3 + \delta S_5\right)\Big|_{i,j,k} \tag{3-30}$$

$S_{1i,j,k}$ is defined by Equation (3-21); $S_{3i,j,k}$ and $S_{5i,j,k}$ are defined by the following:

$$S_{3i,j,k} = \left(\frac{1}{\alpha}\frac{\partial\beta}{\partial y}\frac{\partial\phi}{\partial x} + \frac{1}{\alpha}\beta\frac{\partial^2\phi}{\partial x\partial y} + \frac{1}{\alpha}\frac{\partial\gamma}{\partial y}\frac{\partial\phi}{\partial y} + \frac{1}{\alpha}\frac{\partial\delta}{\partial y}\frac{\partial\phi}{\partial z} + \frac{1}{\alpha}\delta\frac{\partial^2\phi}{\partial y\partial z} - \frac{1}{\alpha}\frac{\partial\sigma_1}{\partial y}\right)\Bigg|_{i,j,k} \tag{3-31}$$

$$S_{5i,j,k} = \left(\frac{1}{\alpha} \frac{\partial \beta}{\partial z} \frac{\partial \phi}{\partial x} + \frac{1}{\alpha} \beta \frac{\partial^2 \phi}{\partial x \partial z} + \frac{1}{\alpha} \frac{\partial \gamma}{\partial z} \frac{\partial \phi}{\partial y} \right.$$

$$\left. + \frac{1}{\alpha} \gamma \frac{\partial^2 \phi}{\partial y \partial z} + \frac{1}{\alpha} \frac{\partial \delta}{\partial z} \frac{\partial \phi}{\partial z} - \frac{1}{\alpha} \frac{\partial \sigma_1}{\partial z} \right) \Bigg|_{i,j,k} . \qquad (3\text{-}32)$$

The boundary conditions imposed on the transport-type equation, either Dirichlet or Neumann, are discretized in the manner described in the previous section.

The algebraic finite-difference equations can be written in the following matrix form:

$$\tilde{C} \, \bar{\phi} = \bar{d} \, . \qquad (3\text{-}33)$$

Unlike the discretized Poisson equation for which the coefficient matrix contains constant elements resulting from the discretized Laplacian, the coefficient matrix for the transport-type equation contains elements which are functions of the flow properties and whose values must be updated during the course of the iteration. Equation (3-33) is solved using Gauss-Seidel line relaxation.

Additional description of the solution of the Poisson-type and transport-type equations is given in the following section.

3.3 The Solution Algorithm for the Coupled System of Equations

The sequence in which the solution of the Poisson- and transport-type equations is carried out is illustrated in Figure 4. Initially the Laplace equation is solved, and the values of Φ are stored for the evaluation of the vector potential, the vorticity, and the turbulent kinetic energy. The calculation of the latter is carried out in the order A_z, Ω_z, A_y, Ω_y, A_x, Ω_x, and k. An inner iteration loop is established in which six of the unknowns are held constant and the seventh is calculated. An outer iteration loop is completed when the inner-loop calculation of all seven variables has been carried out. Following a converged solution for A_1, Ω_1, and k, the Poisson equation for pressure is solved. The pattern of successive line relaxation

which is followed for all the variables is shown in Table 1. For example, with regard to Φ , for a fixed x-y plane, the variable z is set ($\phi_{i,j,k+1}$ and $\phi_{i,j,k-1}$ are transferred to the right side of the equation being solved).

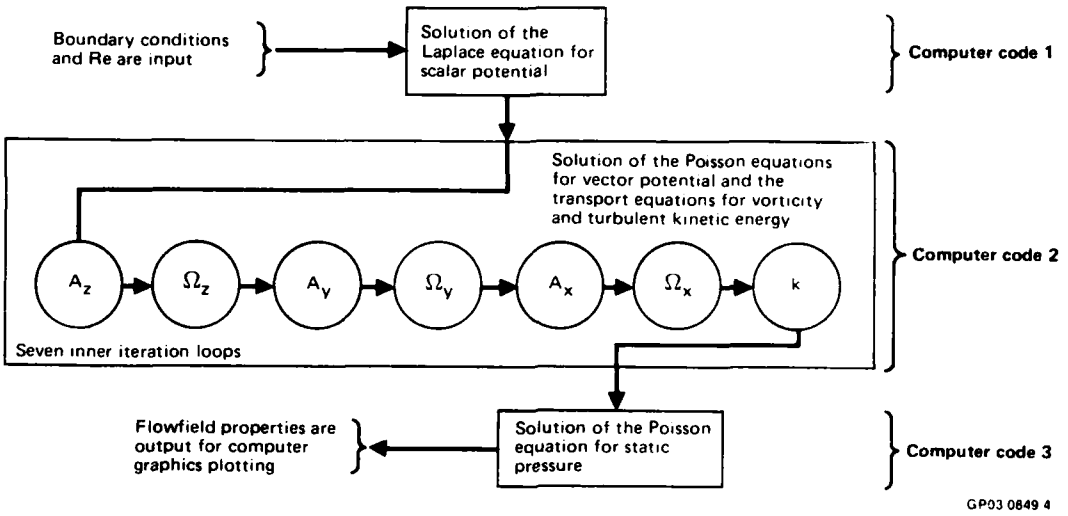

Figure 4. Computing sequence used in the solution of the flowfield equations.

TABLE 1. THE PATTERN OF SUCCESSIVE LINE RELAXATION FOR SOLUTION OF THE FLOWFIELD EQUATIONS.

Dependent variable	First fixed coordinate	Second fixed coordinate	Variable coordinate in successive line relaxation
Φ	z	x	y
A_z	z	x	y
Ω_z	z	x	y
A_y	y	x	z
Ω_y	z	x	y
A_x	x	z	y
Ω_x	z	x	y
k	z	x	y
p	z	x	y

GP03-0849-5

Within the x-y plane, the variable x is then set, which results in a line of ϕ values with y as the variable. This system of equations is solved, and the resulting values are updated using successive line relaxation as x is varied. For all nine flow variables, the final convergence criterion (the difference in magnitude of the unknown between successive iterations) is taken to be 10^{-4}.

The flowfield calculations in the present work were done using the computers of the Systems Technology Program (STP) - System Simulation Center (SSC) operated by the McDonnell Douglas Astronautics Company, Huntington Beach, for the Department of the Army. Jobs were submitted from a Data 100 terminal in MDRL via telephone lines to the STP CDC 6400, which acts as an input/output station and host computer for a CDC 7600. The jobs were batched on the 7600, which is a 65k SCM (small core memory) - 256k LCM (large core memory) configuration. Printed output was generated at MDRL via the Data 100 printer, and tape output was mailed to St. Louis for use with the MDRL computer graphics routines on the McDonnell Douglas Automation Company CYBER 175 computer.

Typical computing times on the 7600 are 1.5 min each for the solution of the Laplace equation for the scalar potential and the Poisson equation for static pressure (approximately 1000 iterations each) and 30-45 min for the solution of the Poisson equations for vector potential and the transport equations for vorticity and turbulent kinetic energy (approximately 120 outer iteration loops). Representative flowfield properties are presented in the next section.

4. THE COMPUTED FLOWFIELDS

Under the present contract, turbulent flowfields induced by interacting impinging jets in ground effect were calculated for the eight configurations defined in Table 2. To illustrate details of the flow property distributions, the computed variables (scalar and vector potential functions, vorticity, velocity, turbulent kinetic energy, and static pressure) were displayed in the form of contour plots on selected planes passing through the computational domain in the three coordinate directions. To provide visualization of the overall flow pattern, three-dimensional pathlines were constructed from the calculated velocity components. In this section, representative contour and pathline plots are presented, and comparisons between computed and measured flow properties are made. A technique for generalizing the boundary conditions in the solution scheme is described.

4.1 Parallel Jets with Normal Impingement

For the case of normal jet impingement, consideration was given to both equal- and unequal-strength jets. In the former case, flowfield solutions were carried out in which the jet height above ground was kept constant (H_c = 4) and the centerline spacing was varied from 5 to 12 (S = 5, 6, 9, and 12). In Figures 5 and 6, contours of Φ, A_x, A_y, A_z, Ω_x, Ω_y, Ω_z, u, v, w, and k are shown on the midplane of the computational domain, y = h/2, for S = 5. The clearest interpretation of the flow pattern

TABLE 2. IMPINGING JET CONFIGURATIONS TREATED IN THE FLOWFIELD COMPUTATIONS.

	Flowfield parameters					Computational domain parameters			
Case	S	H_C	α (deg)	V_{jce_1}/V_{jce_2}	Re	w	h	L	(I, J, K)
1	5	4	90	1.0	100	4	2	5	(17, 9, 21)
2	6	4	90	1.0	100	3	2	6	(13, 9, 25)
3	9	4	90	1.0	100	3	2	9	(13, 9, 37)
4	12	4	90	1.0	100	3	2	12	(13, 9, 49)
5	9	4	90	0.707	100	3	2	9	(13, 9, 37)
6	9	4	90	0.5	100	3	2	9	(13, 9, 37)
7	4.5	4	85	1.0	100	4	2	10.5	(17, 9, 43)
8	8	4	80	0.707	100	3	2	14	(13, 9, 57)

All lengths are normalized by the jet nozzle diameter, and the Reynolds number is based on properties evaluated at the exit plane of nozzle 2.

GP03-0849-20

is given by examination of the plots of the three velocity components, Figures 6(c) - (e), which show the centerline decay and spreading of the primary jets

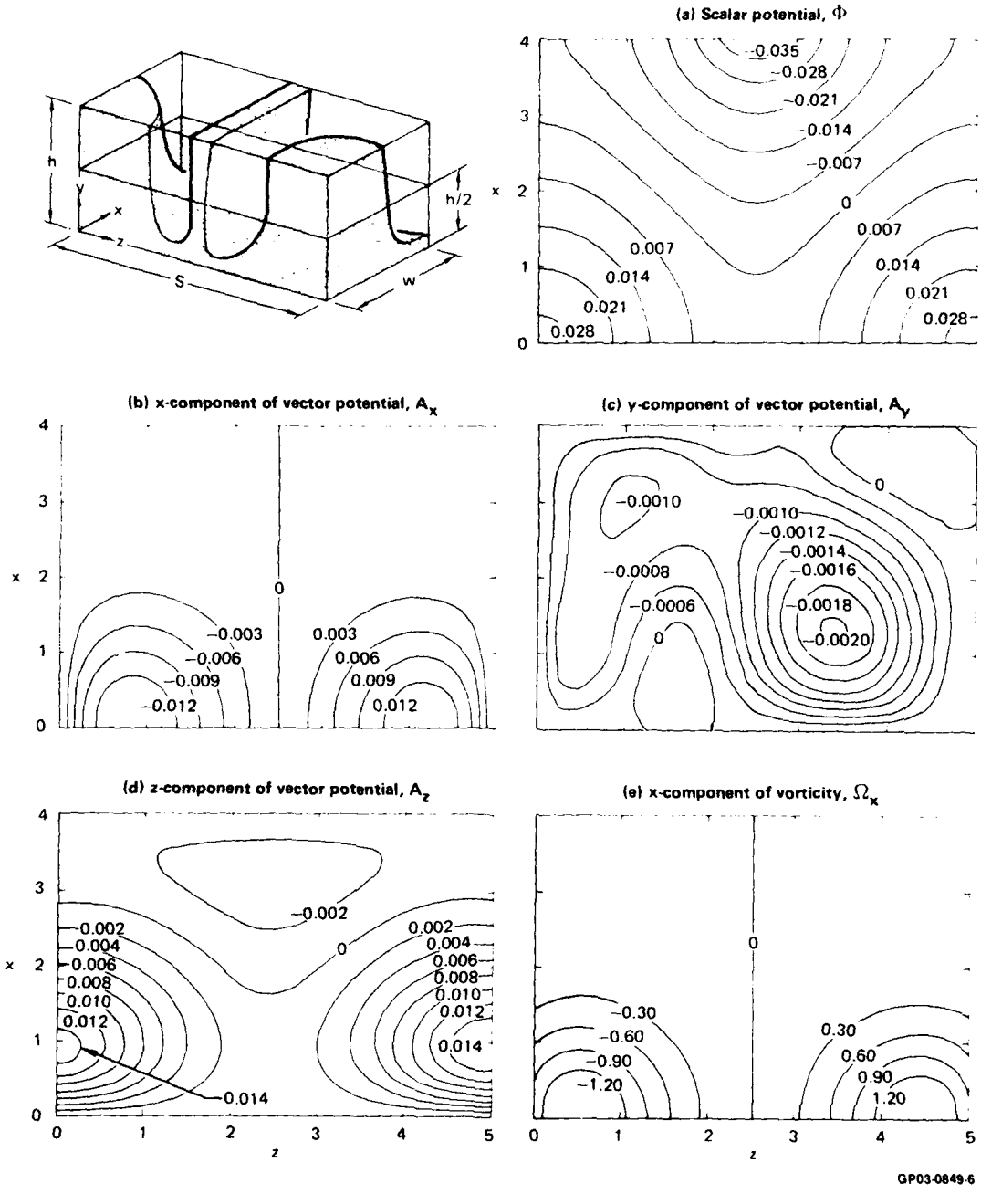

Figure 5. Flowfield properties on the plane y = h/2 for equal-strength jets with normal impingement (S = 5, h = 2, w = 4, Re = 100).

and the entrainment into the fountain. The analogous contour plots for the configurations with S = 6, 9, and 12 are qualitatively the same as those shown in Figures 5 and 6.

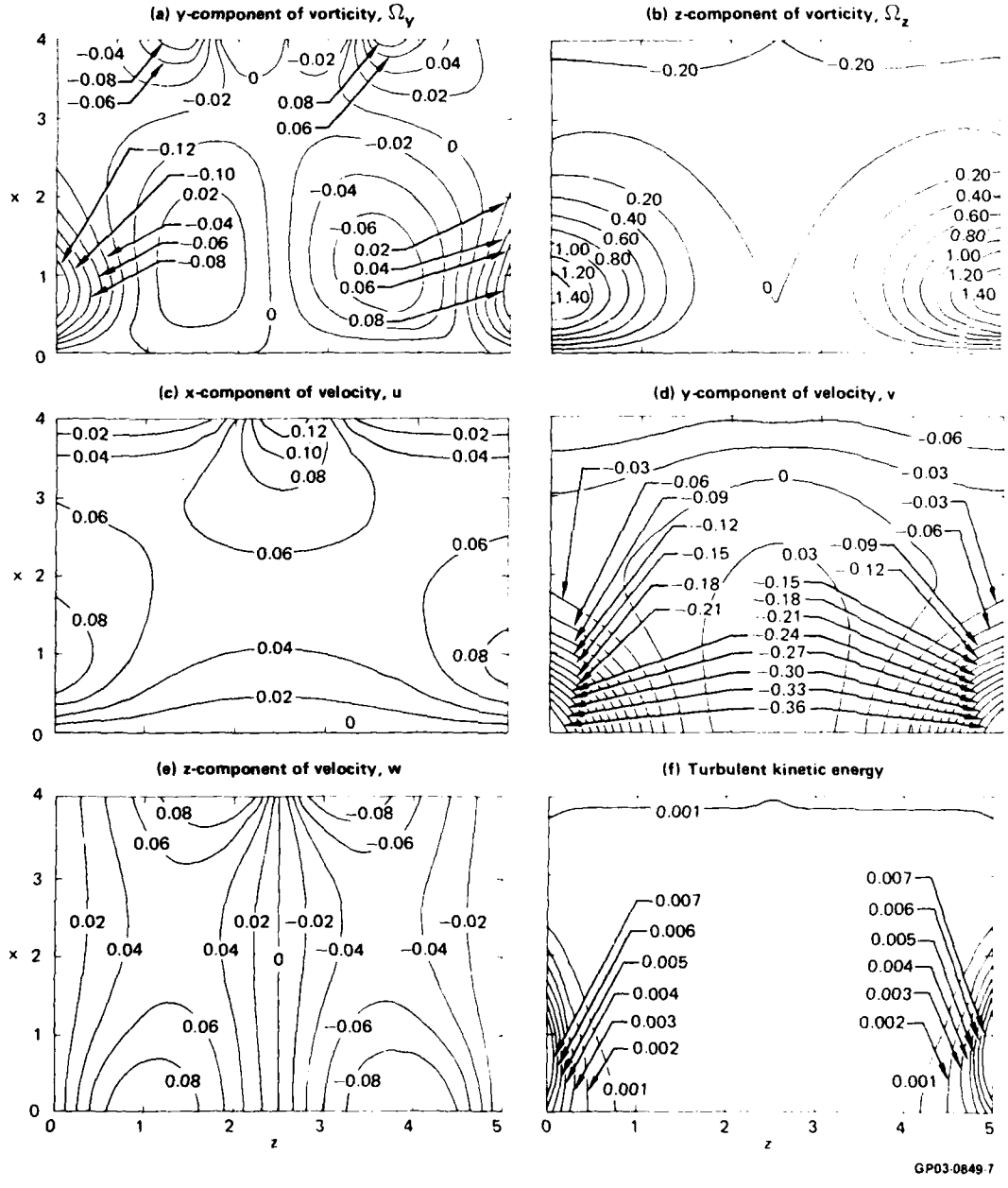

Figure 6. **Flowfield properties on the plane y = h/2 for equal-strength jets with normal impingement (S = 5, h = 2, w = 4, Re = 100).**

Although the planar contour plots provide detailed information about the flow variables throughout the computational region, they do not provide a simple visualization of the overall flow pattern. The physical characteristics of the flowfield are best illustrated through three-dimensional particle-pathline (streamline) traces. These plots are constructed in the following manner: after obtaining a convergent solution of the Navier-Stokes equations, the three components of the velocity vector are stored as a function of position in the computational domain. A point is then selected in the flowfield, and a particle is moved along the local velocity vector at that point over a small time increment. When the particle arrives at a new position, it is again directed along the local velocity vector. This procedure is repeated stepwise in time until the particle exits the computational domain. The CRT graphics routine has the capability of rotating the computational domain about each of the three axes so that the pathlines are visible from any desired angle.

Figure 7 illustrates the streamline plots for the case of equal-strength jets with normal impingement for S = 6, 9, and 12. The origins of the traces are taken to be the nodal points at the periphery of the primary jets on the top surface of the computational domain, as illustrated in the rotated top views of the three configurations. The views at the left in Figure 7 are obtained by rotating the computational domain 45° counterclockwise about the z axis. Shaded areas have been added to the top plane of the computational domain to define the primary jet and fountain regions. These plots clearly show the change in the entrainment flow into the fountain as S is doubled in magnitude.

The accuracy of the computations with regard to the prediction of wall-jet properties for the case of normal impingement is illustrated in Figure 8. The experimental results are for a single turbulent jet striking the ground with $\alpha = 90^{\circ}$, Reference 9, and the computational results are for dual jets with normal impingement and S = 12. For this value of centerline spacing, such a comparison is reasonable. As illustrated in Figure 8(a), the flowfield near the wall is characterized by an impingement region in which the flow changes direction and a wall-jet region in which the shear layer develops over the ground plane.

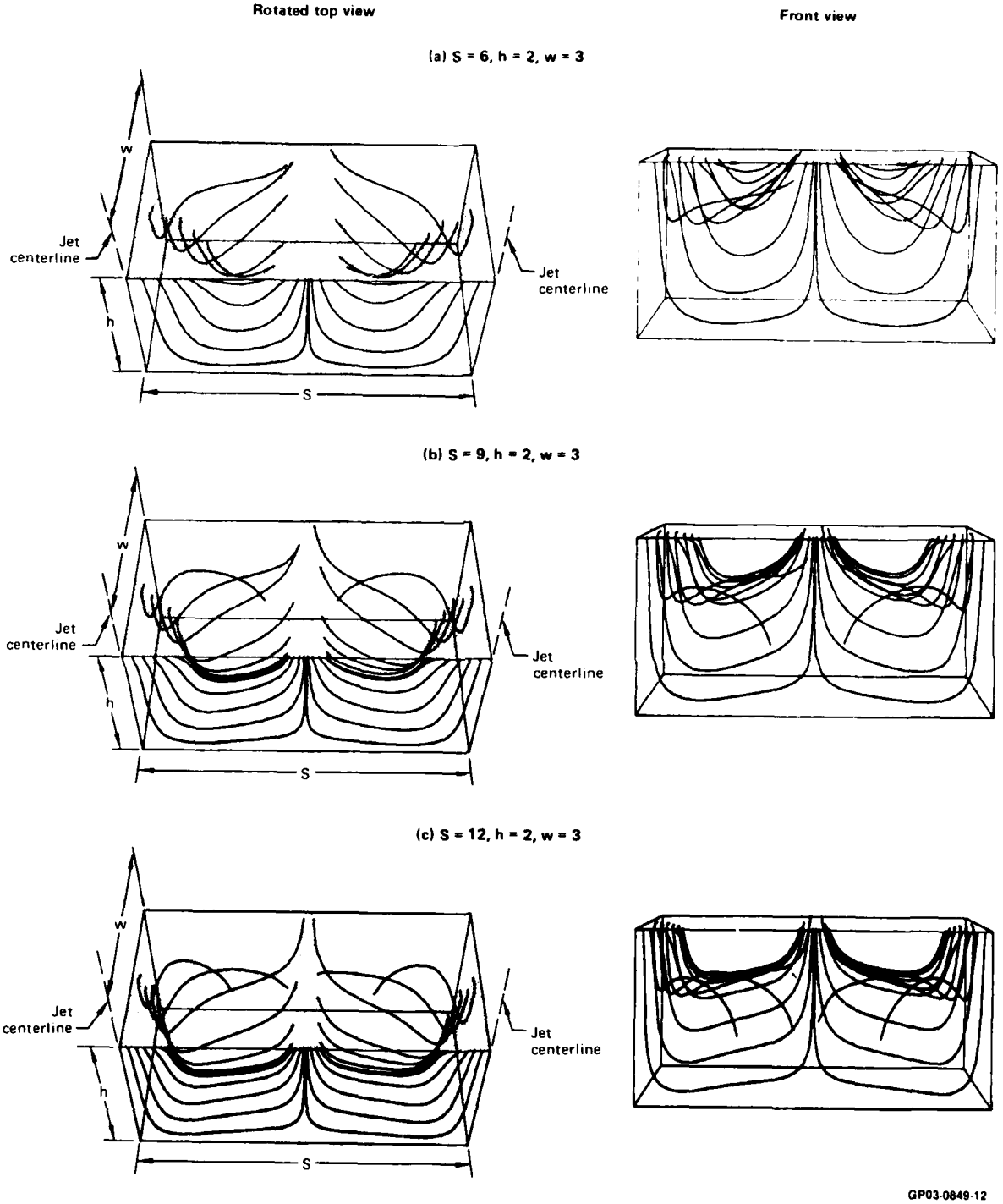

Figure 7. Streamline plots for equal-strength jets with normal impingement (Re = 100).

(a) Schematic illustration of the near-wall regions of an impinging jet flow

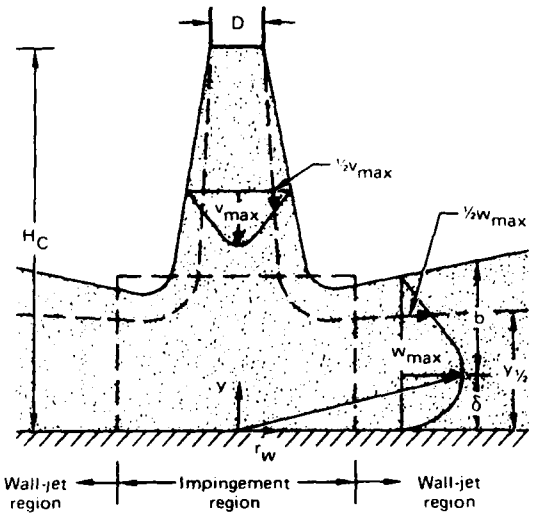

(b) Computed wall-jet velocity profile and comparison with Abramovich's relation (Reference 9) outside the inner turbulent boundary layer

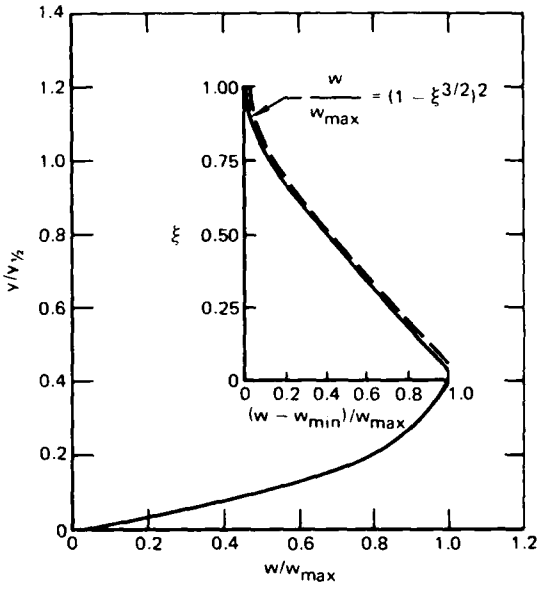

(c) Measured variation of maximum wall-jet velocity with distance from the stagnation point (Reference 9)

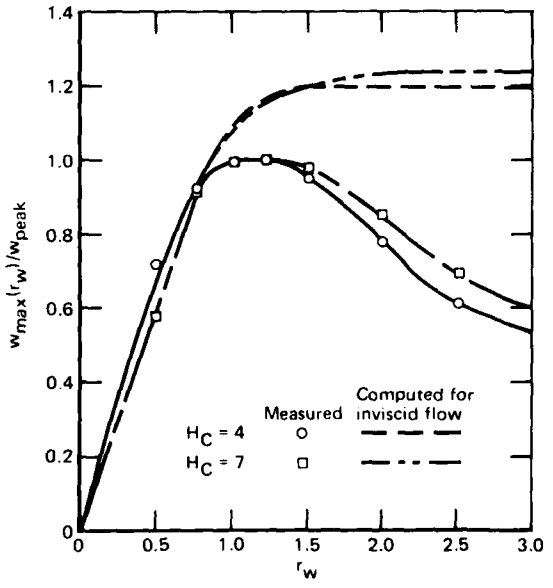

(d) Computed variation of maximum wall-jet velocity with distance from the stagnation point (Reference 9)

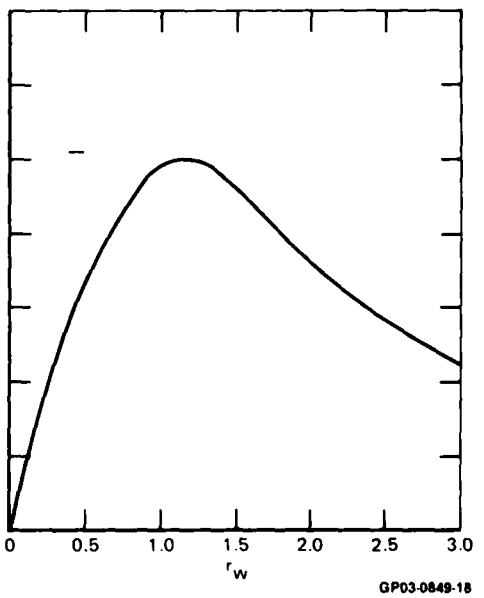

GP03-0849-18

Figure 8. Comparison of computed and measured wall-jet properties for normal jet impingement.

A velocity profile computed in the wall-jet region is shown in Figure 8(b) in which w/w_{max} is plotted as a function of $y/y_{1/2}$, where $y_{1/2}$ is the value of y for which $w/w_{max} = 0.5$. Outside the inner turbulent boundary layer ($y > \delta$), Abramovich's relation for the velocity profile, Reference 9, is applicable.

$$\frac{w}{w_{max}} = (1 - \xi^{3/2})^2, \tag{4-1}$$

where $\xi = (y - \delta)/b$, with b denoting the distance between the point of maximum velocity and the edge of the shear layer. Equation (4-1) and the profile obtained from the Navier-Stokes equations coincide.

Figure 8(c) shows the measured variation (Reference 9) of the maximum wall-jet velocity with distance from the stagnation point for two values of jet height above ground, $H_c = 4$ and 7. The local maximum velocity $w_{max}(r_w)$ for a given distance from the stagnation point is normalized by the largest value of w_{max} for the entire range of r_w, a value denoted by w_{peak}. In the vicinity of the stagnation point (r_w less than approximately 1), viscous effects are negligible and $w_{max}(r_w)/w_{peak}$ varies essentially linearly with r_w. As r_w increases beyond unity, viscous effects increase and the maximum wall-jet velocity decays. In the absence of dissipation, the curves would continue to increase to an asymptotic value, as shown by the inviscid flow curves which were obtained from Bernoulli's equation. The variation of $w_{max}(r_w)/w_{peak}$ given by the Navier-Stokes equations shows a trend identical to that observed experimentally.

The computed pressure distribution on the ground plane line $x = 0$ is shown in Figure 9(a) for the case of dual-jet impingement with $S = 12$ and $Re = 100$. Also shown on the plot are the data of Jenkins and Hill, Reference 10, which were measured for the same configuration but with a Reynolds number on the order of 10^5. The jets stagnate on the ground, deflect 90^o, spread as radial wall jets, and then collide at the midplane between the jet centerlines to form the upwash flow. The measured pressure profile shows a rapid decay from the stagnation point value, an essentially constant ambient level through the wall jet, and a rise in the collision zone as the flow decelerates in the

(a) Ground pressure distribution for equal-strength jets with normal impingement, x = 0 (S = 12, h = 2, w = 3, Re = 100)

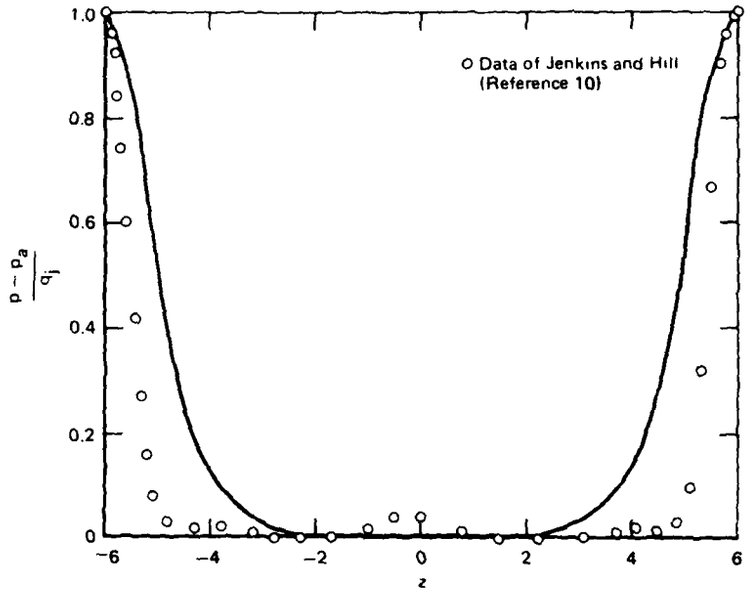

(b) Flow direction in the midplane of the fountain for equal-strength jets with normal impingement (h = 2, w = 3, Re = 100)

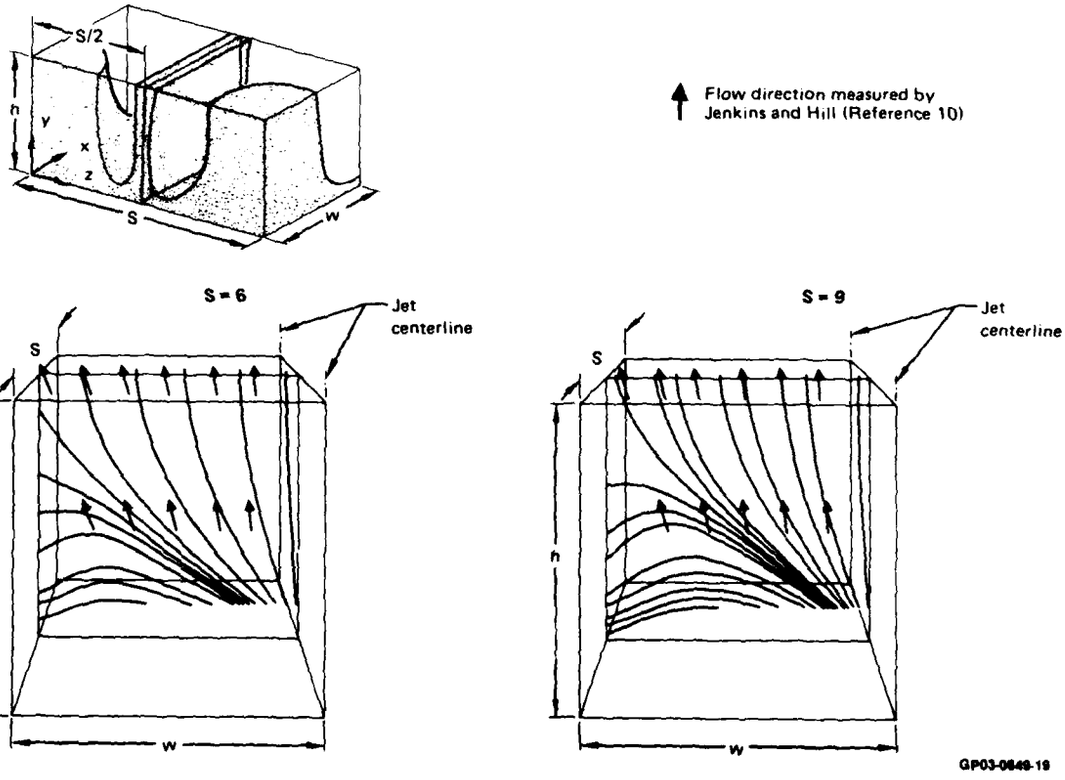

Figure 9. Comparison of computed and measured flow properties for equal-strength jets with normal impingement.

horizontal direction and turns in the vertical direction. The computed pressure rise does not demonstrate the same decay rate from the peak pressure nor the rise in the collision zone. This discrepancy is attributed primarily to the inability of the relatively coarse grid used in the finite-difference calculations to adequately represent the velocity gradients in the impingement and upwash regions.

Also shown in Figure 9 is a comparison of the computed and measured flow directions in the midplane of the fountain for equal-strength jets with S = 6 and 9. Most zonal analysis schemes which are used to model the upwash for interacting jets are based on the assumption that the radial flow pattern of the wall jets on the ground plane is continued into the upwash, with the virtual origin taken to be a distance S/2 below the ground. The flow direction was determined by Jenkins and Hill, Reference 10, using an array of 17 flags in the plane z = S/2 which were mounted on a ladder-shaped wire support permitting each flag to pivot in the x direction. Photographs taken to show the flow direction and used to construct the arrows in Figures 9(b) and (c) indicate that the assumption of radial flow is a good one except in regions far from the central upwash, a condition which Jenkins and Hill attribute to entrainment and turbulent mixing of ambient air into the upwash. The comparison of the experimental flow direction with the computed streamlines shows that the latter give a good representation of the flow direction except near the outflow plane x = w where the streamlines are forced to intersect the surface in a direction set by the imposed boundary conditions.

Particle pathline plots computed for unequal-strength jets with normal impingement are shown in Figure 10. In this case the jet centerline spacing was held constant, and the momentum ratio at the exit plane of the two jets was varied over the range M_1/M_2 = 1.0, 0.5, and 0.25. These momentum ratios correspond to jet centerline velocity ratios of V_{jce_1}/V_{jce_2} = 2.0, 0.707, and 0.5. With the primary jet and fountain regions shaded in the rotated top view of the computational domain, the pathline plots show the shift in the fountain toward the weaker jet and the strong interaction between the latter and the upwash.

The location of the stagnation line resulting from the collision of the opposing wall jets is indicated by the contours of the z-component of velocity

one grid space above the ground plane given in Figure 11. The flow conditions are the same as those in the streamline plots of Figure 10. For the lowest

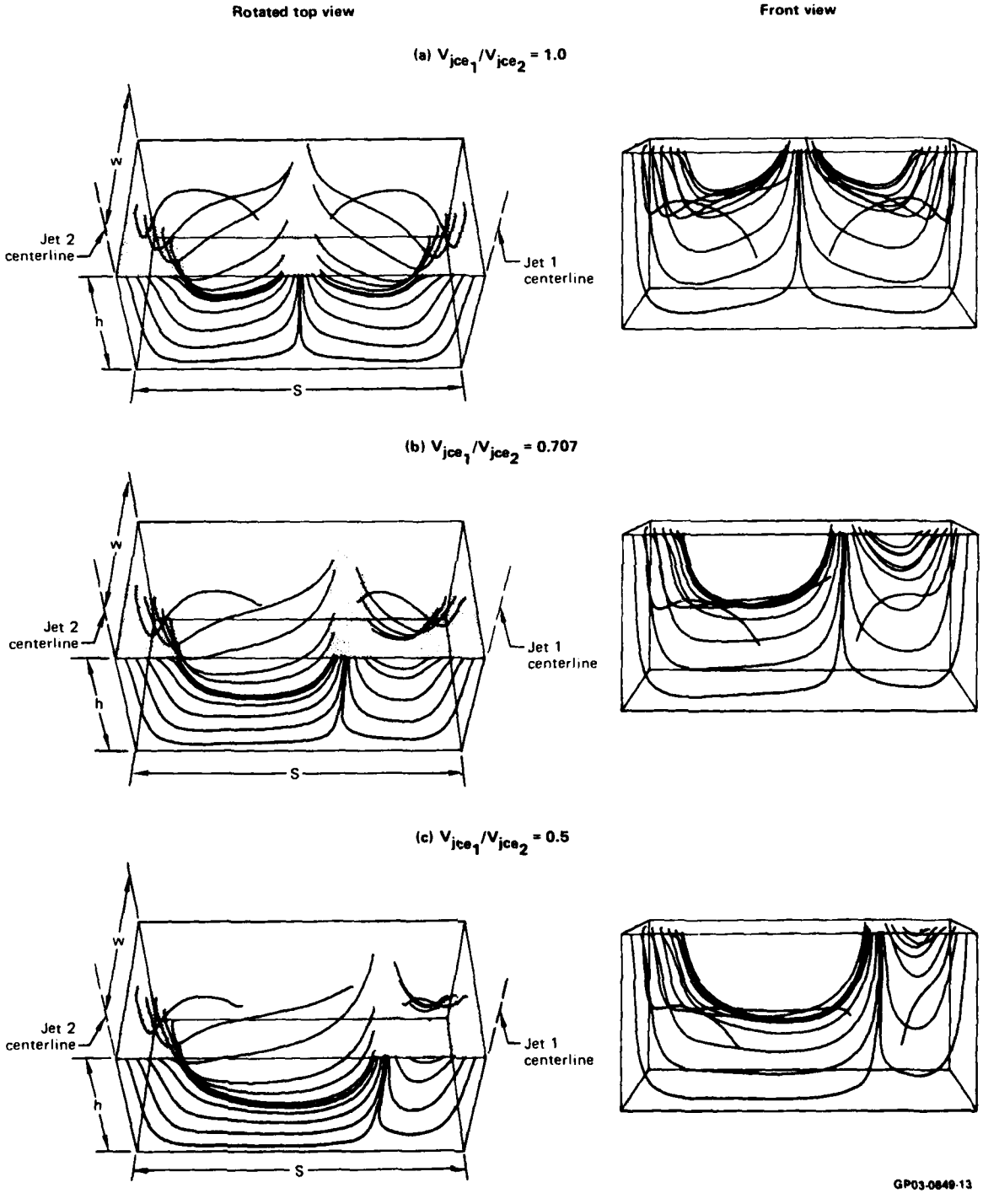

Figure 10. Streamline plots for unequal-strength jets with normal impingement (s = 9, h = 2, w = 3, Re = 100).

velocity ratio, there is a displacement of approximately one diameter in the w = 0 line from the midpoint between the jet centerlines.

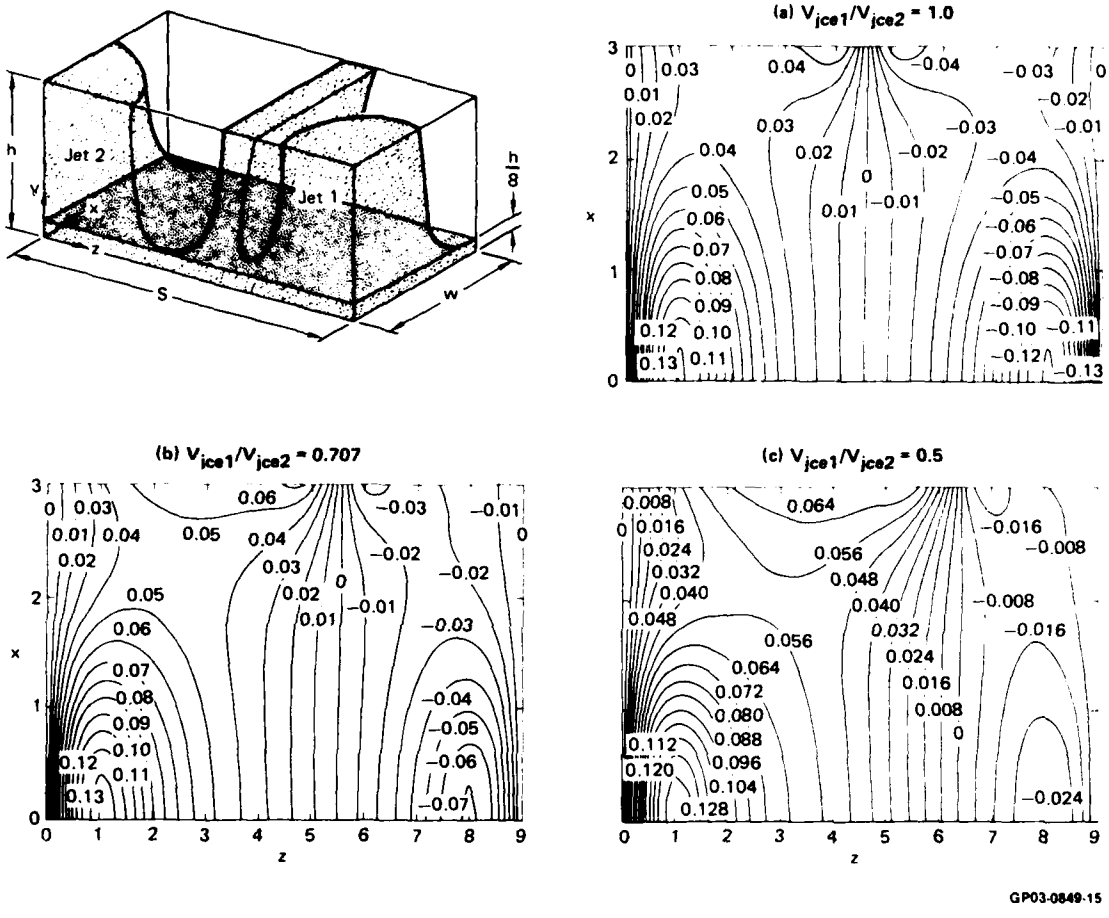

Figure 11. Contours of the z-component of velocity on the plane y = h/8 for unequal-strength jets with normal impingement (S = 9, h = 2, w = 3, Re = 100).

4.2 Parallel Jets with Inclined Impingement

For the case of inclined jet impingement, flowfield calculations were carried out for both equal- and unequal-strength jets. Contour plots of the computed flow variables for equal-strength jets with S = 4.5, L = 10.5, and $\alpha = 85^{o}$ are shown in Figures 12 and 13 for the midplane y = h/2 of the computational domain. Jenkins and Hill, Reference 10, do not report a measured ground-plane pressure distribution for this configuration, but they do provide an experimental ground-plane stagnation line which is compared with the computed line in Figure 14.

A calculation of unequal-strength jets with inclined impingement was made for a configuration with S = 8, L = 14, $\alpha = 80^{o}$, and $V_{jce_1}/V_{jce_2} = 0.707$. Figure 15 shows contours of the y-component of velocity on three x-z planes in the computational domain (y = 0.33, 1.67, and 2) which demonstrate the computed variation in the primary jet velocity profiles as the ground plane is approached.

4.3 Planar Flowfields Computed with Coordinate Transformations

A shortcoming in the present flowfield prediction scheme for three-dimensional, interacting, impinging jets with fountain formation is the rather involved procedure for specifying boundary conditions. This approach, outlined in Appendix A, requires empirical data and numerous engineering approximations regarding the characteristics of the flow. A better technique is to remove the computational boundaries from the near field and place them in the far field where simple conditions, such as no property gradients in the primary flow direction, can be meaningfully imposed. This approach can be adopted through the use of coordinate transformations to map a relatively large physical domain into a smaller computational domain.

An exploratory study of transforming the coordinates in the Navier-Stokes equations was investigated by Dr. R. K. Agarwal (MDRL) under the present contract. An Euler transformation was used to map the physical-domain variables (x, y) into the computational-domain variables $(\bar{x}, \bar{y})$,

$$\bar{x} = \frac{x}{1 + Px}, \qquad \bar{y} = \frac{y}{1 + Qy} . \tag{4.2}$$

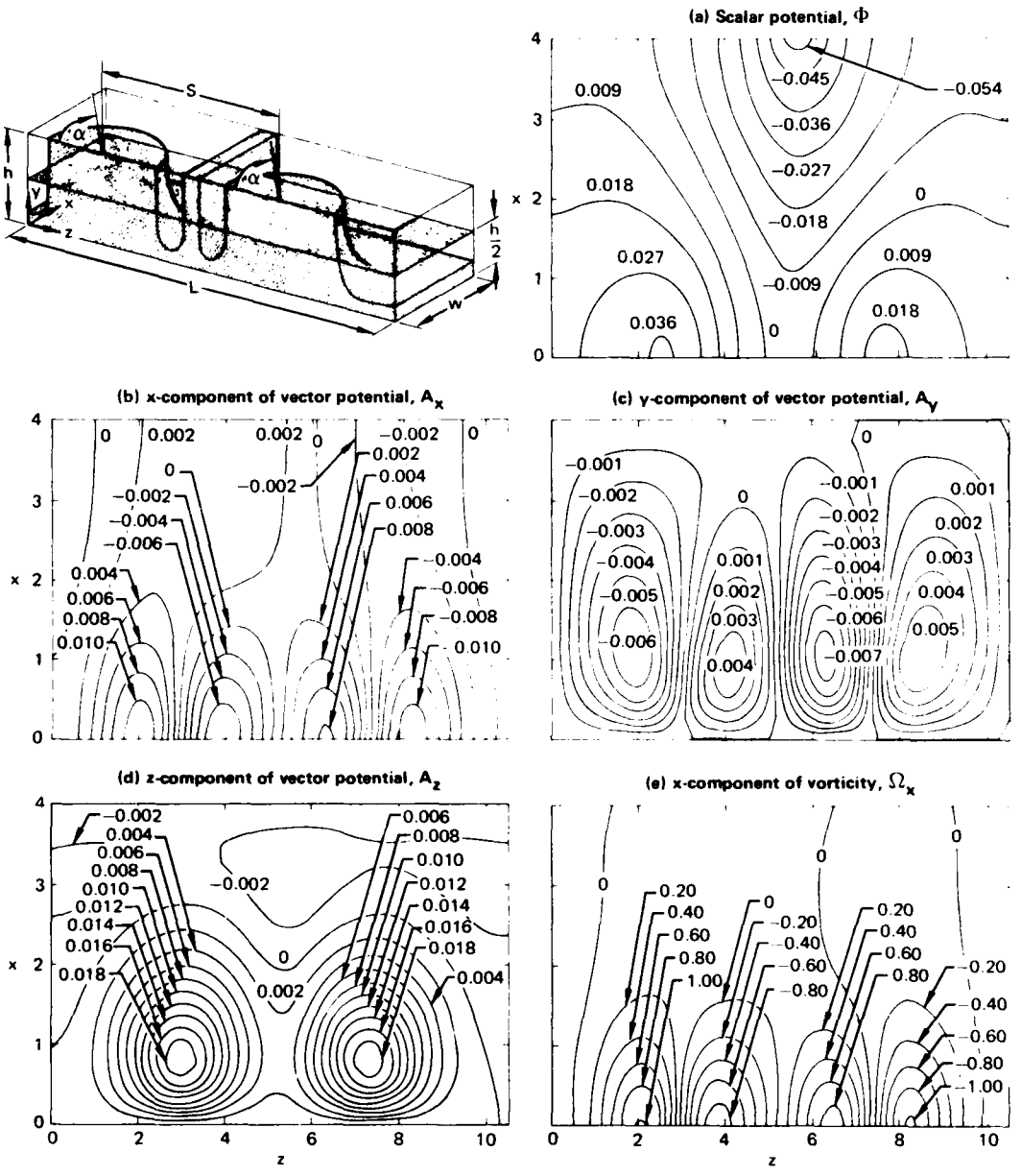

Figure 12. Flowfield properties on the plane y = h/2 for equal-strength jets with inclined impingement (S = 4.5, L = 10.5, α = 85°, h = 2, w = 4, Re = 100).

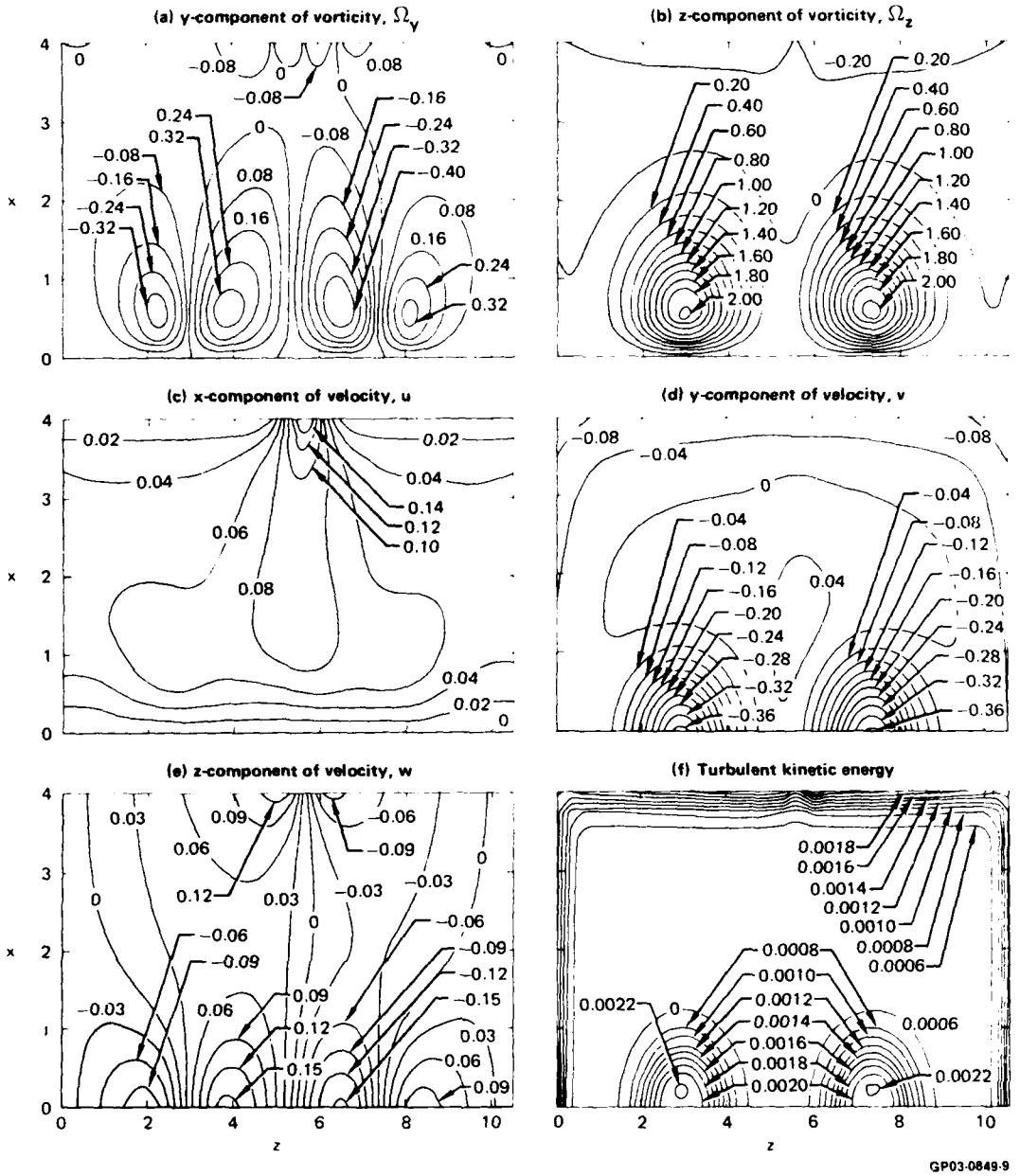

Figure 13. Flowfield properties on the plane y = h/2 for equal-strength jets with inclined impingement (S = 4.5, L = 10.5, α = 85°, h = 2, w = 4, Re = 100).

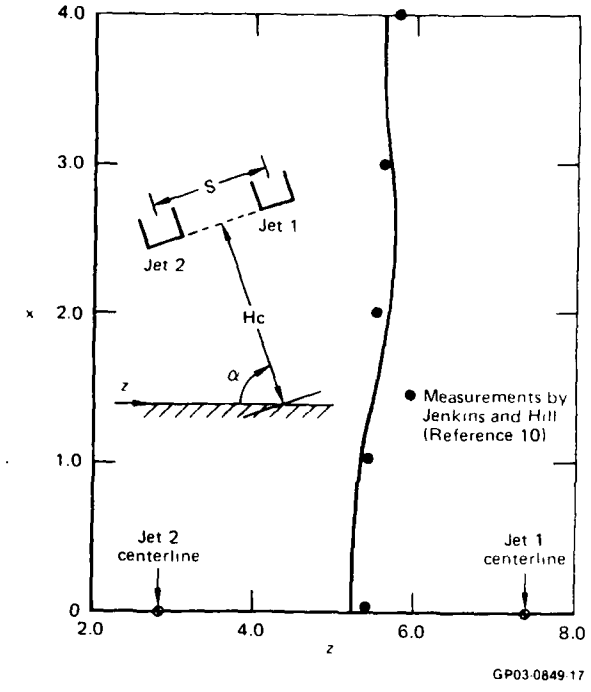

Figure 14. Comparison of measured and computed stagnation line shape for equal-strength jets with inclined impingement ($S = 4.5$, $H_c = 2.74$, $\alpha = 85°$, $Re = 100$).

The constants P and Q were chosen to obtain the desired clustering of grid points in different regions of the physical domain. For simplicity, the coordinate transformation scheme was applied to the two-dimensional, time-averaged Navier-Stokes and turbulence model equations described in Reference 3 rather than to the three-dimensional equations. The Poisson equation for the stream function and the transport equations for vorticity, turbulent kinetic energy, and turbulent dissipation were written in the transformed coordinates $(\bar{x}, \bar{y})$ and solved using the augmented-central-difference (ACD) algorithm.

Computations were carried out for the following three cases: laminar entry flow in a channel, impingement on a flat plate of a planar laminar jet with a free upper boundary, and impingement on a flat plate of a planar turbulent jet with a free upper boundary. Flow properties computed for these geometries are shown in Figure 16. For the laminar entry flow (Re = 75), a fully developed condition was assumed 100 channel widths downstream of the

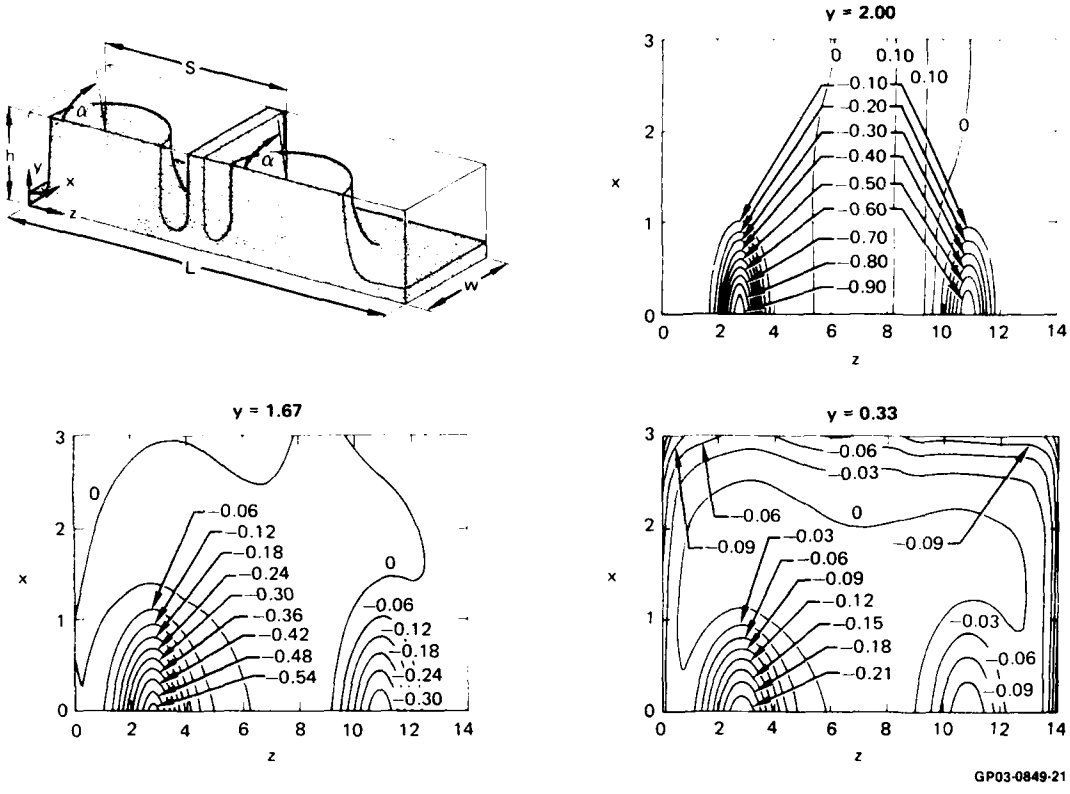

Figure 15. Contours of the y-component of velocity for unequal-strength jets with inclined impingement (S = 8, L = 14, α = 80°, h = 2, w = 3, Re = 100).

entrance plane, and Equation (4-2) was applied with P = 99/100 and Q = 0. Figure 16(a) shows the variation of the centerline velocity along the channel axis and the excellent agreement with the computations of Wang and Longwell, Reference 11. For the laminar impinging jet, the solution was carried out with the nozzle exit plane located a distance $H_c/D = 40$ above the ground plane and with $Re = 10^3$. In the transformation given by Equation (4-2), $P = Q = 39/40$. The surface vorticity, which is shown in Figure 16(b), assumes a constant value in approximately three jet widths from the stagnation point. For the turbulent impinging jet solution, $H_c/D = 31$, $Re = 5.3 \times 10^3$, and $P = Q = 30/31$. Figure 16(c) illustrates the ground plane vorticity.

The coordinate transformation work with the Navier-Stokes equations for planar flow has demonstrated the feasibility of extending the procedure to the three-dimensional impinging jet configurations with fountain formation.

(a) Velocity variation along the centerline for a laminar duct flow

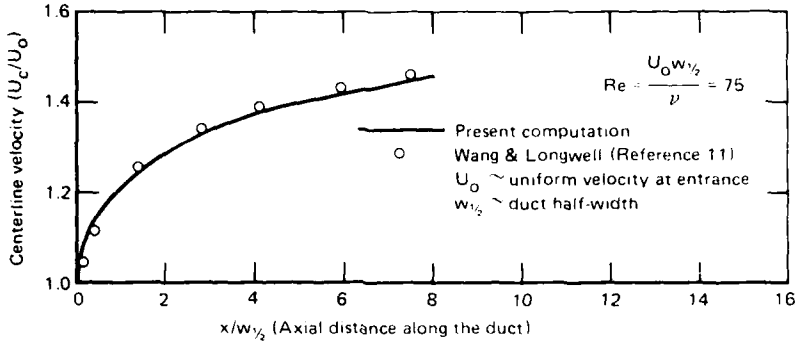

(b) Vorticity variation along the plate in the impingement region for a laminar jet

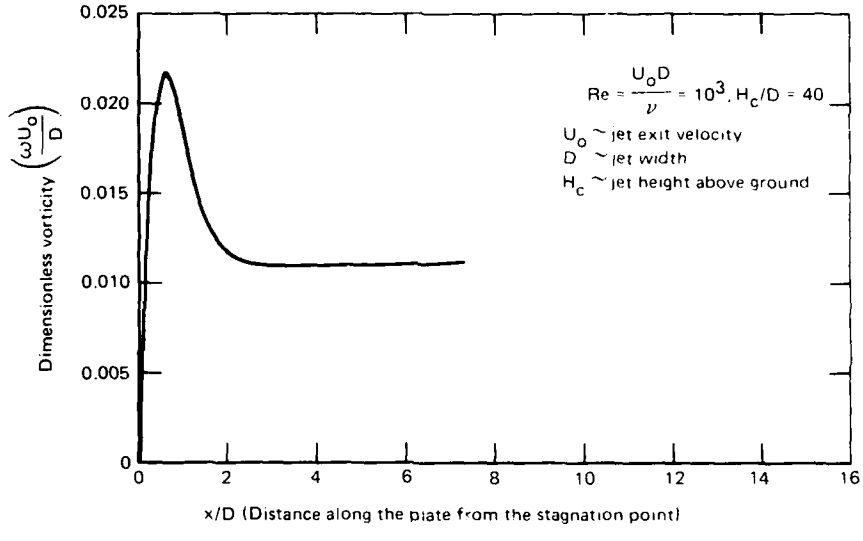

(c) Vorticity variation along the plate in the impingement region for a turbulent jet

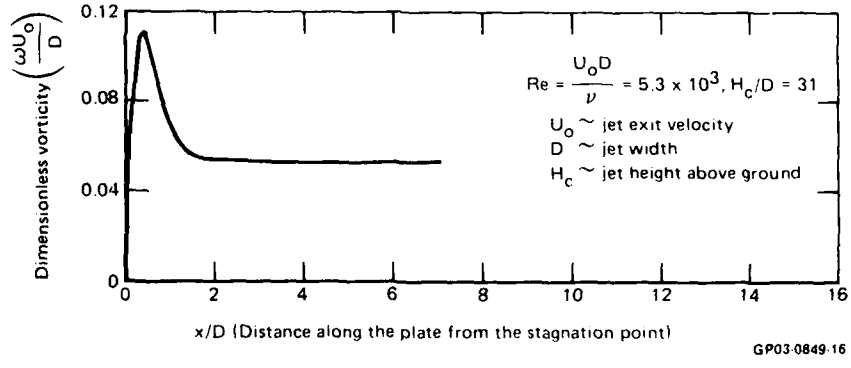

Figure 16. Computed properties for two-dimensional duct and jet impingement flows obtained using coordinate transformations.

5. SUMMARY

Starting with the complete elliptic conservation equations for incompressible, steady, three-dimensional viscous flow, a flowfield model has been formulated and solved numerically for two parallel jets which impinge on a ground plane and interact to form a fountain upwash. The time-averaged Navier-Stokes equations in combination with the Glushko turbulence model are cast in terms of Poisson equations for scalar and vector potential functions and static pressure and in terms of transport equations for vorticity and turbulent kinetic energy. This system was solved using finite-difference procedures for eight two-jet configurations with various centerline spacings, angles of inclination, and nozzle exit-plane velocity ratios. In this section, the characteristics of the numerical scheme and computed flowfields are summarized, and recommendations are made for generalizing and improving the accuracy of the prediction method.

5.1 Conclusions

With regard to the numerical solution scheme, no significant problems were encountered in obtaining convergent solutions of the coupled system of equations for the conditions defined in Table 2. The computed flowfields provide reasonable prediction of the wall-jet characteristics, the upwash flow direction, and the stagnation line patterns on the ground plane. However, the ground-plane pressure profiles do not predict the experimental variation in the stagnation zones of the impinging primary jets and the colliding wall jets.

The limitations of the present prediction method, which are common to most Navier-Stokes steady-state finite-difference schemes applied to complex three-dimensional flows, are the following:

(1) The use of empirically determined boundary conditions in the near field. In the present work, the rather involved procedure outlined in Appendix A for setting the near-field boundary conditions is necessary. This approach requires the use of empirical data to establish the velocity profiles through the wall jets and fountain on the boundary planes of the computational domain. A oetter approach is to take the computational boundaries in the far field where simple

constraints are valid, such as no gradients in the fluid properties in the outflow direction.

(2) The use of coarse grids imposed by computer storage constraints. In the present work, the same grid spacing h (the distance between nodal points in the finite-difference mesh) is used in all three coordinate directions. Consequently, for a given computational domain, if the grid spacing is decreased by a factor of two, for example, to obtain a greater resolution in one coordinate direction, h must be divided by two in the remaining coordinate directions. This procedure essentially doubles the number of grid points in each coordinate direction, which means increasing by a factor of eight the number of storage locations required for each triply dimensioned variable. In the present code there are 20 arrays with dimensions (I, J, K) with the result that halving the grid spacing increases the dimensioning of these variables by a factor of 160. Consequently, an improved approach is to permit specification of the node spacing independently in each of the three coordinate directions. Moreover, there is a need to nonuniformly cluster the grid points within a given coordinate direction so that the regions of the flow where property gradients are the largest (such as the wall-jet regions near the stagnation zones) can be computed with greater resolution. This approach should also permit solutions to be carried out at a Reynolds number several orders of magnitude larger than that considered in the present study.

5.2 Recommendations

The two limitations described previously can be removed through the use of coordinate transformations to permit the application of the boundary conditions in the far field and to permit clustering of the grid points in regions of large property gradients.

With regard to the specification of the boundary conditions, the objective of the transformation is to map a large (even infinite) physical domain for which the boundary conditions are known into a smaller computational domain which can be adequately represented by a finite number of grid points. With regard to improving the resolution of the flowfield,

coefficients can be introduced into the coordinate transformations which permit clustering the grid points in regions of large property gradients. As pointed out by Oberkampf, Reference 12, by transforming to a computational plane which "stretches" regions of large property gradients in the physical plane and "compresses" regions of small property gradients in the physical plane, it is possible to reduce the truncation error of the finite-difference solution. Generally, the computations can be carried out more efficiently and for a higher Reynolds number than can be done using a relatively coarse uniform grid.

Under contract to ONR, MDRL will use coordinate transformations in solution of the three-dimensional time-averaged Navier-Stokes and turbulence model equations. In addition, the augmented-central-difference (ACD) discretization scheme used in the work presented in this report will be replaced by an upwind difference scheme to eliminate the storage of the triply dimensioned arrays α, β, γ, and δ [Equation (3-16)] required in the ACD algorithm. The upwind difference formulation will permit more grid points to be used to better resolve the flowfield. Calculations will be made for equal- and unequal-strength jets with normal and inclined impingement.

REFERENCES

1. D. R. Kotansky, N. A. Durando, D. R. Bristow, and P. W. Saunders, Multi-Jet Induced Forces and Moments on VTOL Aircraft Hovering In and Out of Ground Effect, Report No. NADC-77-229-30, Naval Air Development Center, 19 June 1977.
2. M. J. Siclari, W. G. Hill, Jr., and R. C. Jenkins, Investigation of Stagnation Line and Upwash Formation, AIAA Paper No. 77-615, AIAA/NASA Ames V/STOL Conference, June 1977.
3. W. W. Bower, R. K. Agarwal, G. R. Peters, and D. R. Kotansky, Viscous Flowfields Induced by Two- and Three-Dimensional Lift Jets in Ground Effect, Report No. ONR-CR215-246-3F, Office of Naval Research, 1 March 1979.
4. M. J. Siclari, W. G. Hill, Jr., R. C. Jenkins, and D. Migdal, VTOL In-Ground Effect Flows for Closely Spaced Jets, AIAA Paper No. 80-1880, AIAA Aircraft Systems Meeting, August 1980.
5. G. S. Glushko, Turbulent Boundary Layer on a Flat Plate in an Incompressible Fluid, NASA TT F-10,080, translation from Izvestiya Akademii Nauk SSSR, Seriya Mekhanika, No. 4, 13 (1965).
6. Y. A. S. Aregbesola and D. M. Burley, The Vector and Scalar Potential Method for the Numerical Solution of Two- and Three-Dimensional Navier-Stokes Equations, J. Comp. Phys. 24, 398 (1977).
7. G. J. Hirasaki and J. D. Hellums, Boundary Conditions on the Vector and Scalar Potentials in Viscous Three-Dimensional Hydrodynamics, Quart. Appl. Math. 28, 293 (1970).
8. G. H. Hoffman, Calculation of Separated Flows in Internal Passages, Proceedings of a Workshop on Prediction Methods for Jet V/STOL Propulsion Aerodynamics 1, 114 (1975).
9. P. Hrycak, D. T. Lee, J. W. Gauntner, and J. N. B. Livingood, Experimental Flow Characteristics of a Single Turbulent Jet Impinging on a Flat Plate, NASA TN D-5690, March 1970.
10. R. C. Jenkins and W. G. Hill, Jr., Investigation of VTOL Upwash Flows Formed by Two Impinging Jets, Grumman Research Department Report RE-548, November 1977.

11. Y. L. Wang and P. A. Longwell, Laminar Flow in the Inlet Section of Parallel Plates, AIChE J. 10, 323 (1964).

12. W. L. Oberkampf, Domain Mappings for the Numerical Solution of Partial Differential Equations, Intl. J. Numerical Methods Eng. 10, 211 (1976).

13. C. du P. Donaldson and R. S. Snedeker, A Study of Free Jet Impingement, Part I - Mean Properties of Free and Impinging Jets, J. Fluid Mech. 45, 281 (1971).

14. L. J. S. Bradbury, The Impact of an Axisymmetric Jet onto a Normal Ground, Aeronautical Quart. 23, 141 (1972).

15. R. C. Jenkins and W. G. Hill, Jr., Investigation of the Effects of Close Nozzle Spacing on Upwash and Fountain Formation, Proceedings of a Workshop on V/STOL Aircraft Aerodynamics 1, 386 (1979).

APPENDIX A: DEFINITION OF THE VELOCITY BOUNDARY CONDITIONS FOR THE THREE-DIMENSIONAL JET IMPINGEMENT CONFIGURATIONS

This appendix presents details of the calculation of the velocity profiles normal to the surfaces of the computational domain for the most general case of interest in the present analysis, unequal-strength jets with inclined impingement. The simplifications in the specification of boundary conditions for the case of normal impingement of two jets are noted.

Consider the configuration shown in Figure 17. Both jets have a nozzle exit diameter D, and H_c denotes the distance from the nozzle exit plane to the midpoint of the distance between the centerline intercepts with the ground plane. The angle of inclination of each jet is α_{jI}, and the nozzle centerline separation distance is S. The computational domain, indicated by the dashed lines, has dimensions w, h, and L in the x, y, and z directions, respectively. For the definition of the velocity boundary conditions, the origin has been shifted from the left boundary to the center of the computational domain.

First, consider the specification of the velocity profiles in the entering jets at the top surface of the computational domain, y = h. Bradbury's profile based on experimental results, Reference 14, is used in which the velocity variation V through the jet normalized by the centerline value V_{jc} is given by

$$\frac{V}{V_{jc}} = \exp\left[-0.6749\eta_j^2\left(1 + 0.0269\eta_j^4\right)\right], \qquad \text{(A-1)}$$

where $\eta_j = r_j/\delta$, r_j is the radial coordinate from the jet centerline, and δ is the value of r_j at which $V = 0.5\ V_{jc}$. A plot of this profile is shown in Figure 18(a). V_{jc} and δ are obtained from the empirical curve fits shown in Figure 18(b) of V_{jc}/V_{jce} and δ/y'' as functions of y''/D. V_{jce} is the nozzle-exit-plane jet centerline velocity, and y" is a coordinate perpendicular to the nozzle exit plane.

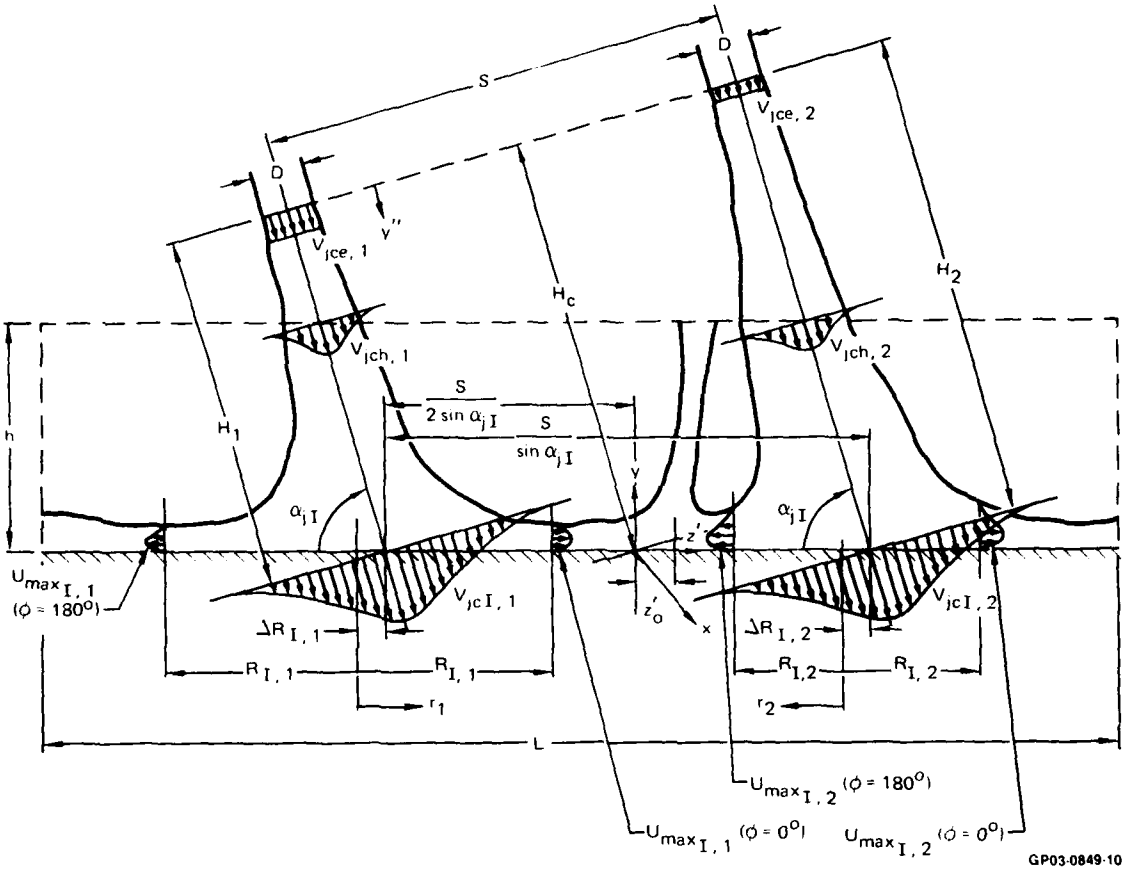

Figure 17. Definition of the flowfield parameters for two jets of equal or unequal strength with inclined impingement on a ground plane.

In the configuration of Figure 17, the distance from the exit plane of nozzle 1 to the point where the geometric centerline intercepts the ground plane is given by

$$H_1 = H_c - \frac{S \operatorname{ctn} \alpha_{jI}}{2} . \qquad \text{(A-2)}$$

Similarly, the corresponding distance from nozzle 2 is

$$H_2 = H_c + \frac{S \operatorname{ctn} \alpha_{jI}}{2} . \qquad \text{(A-3)}$$

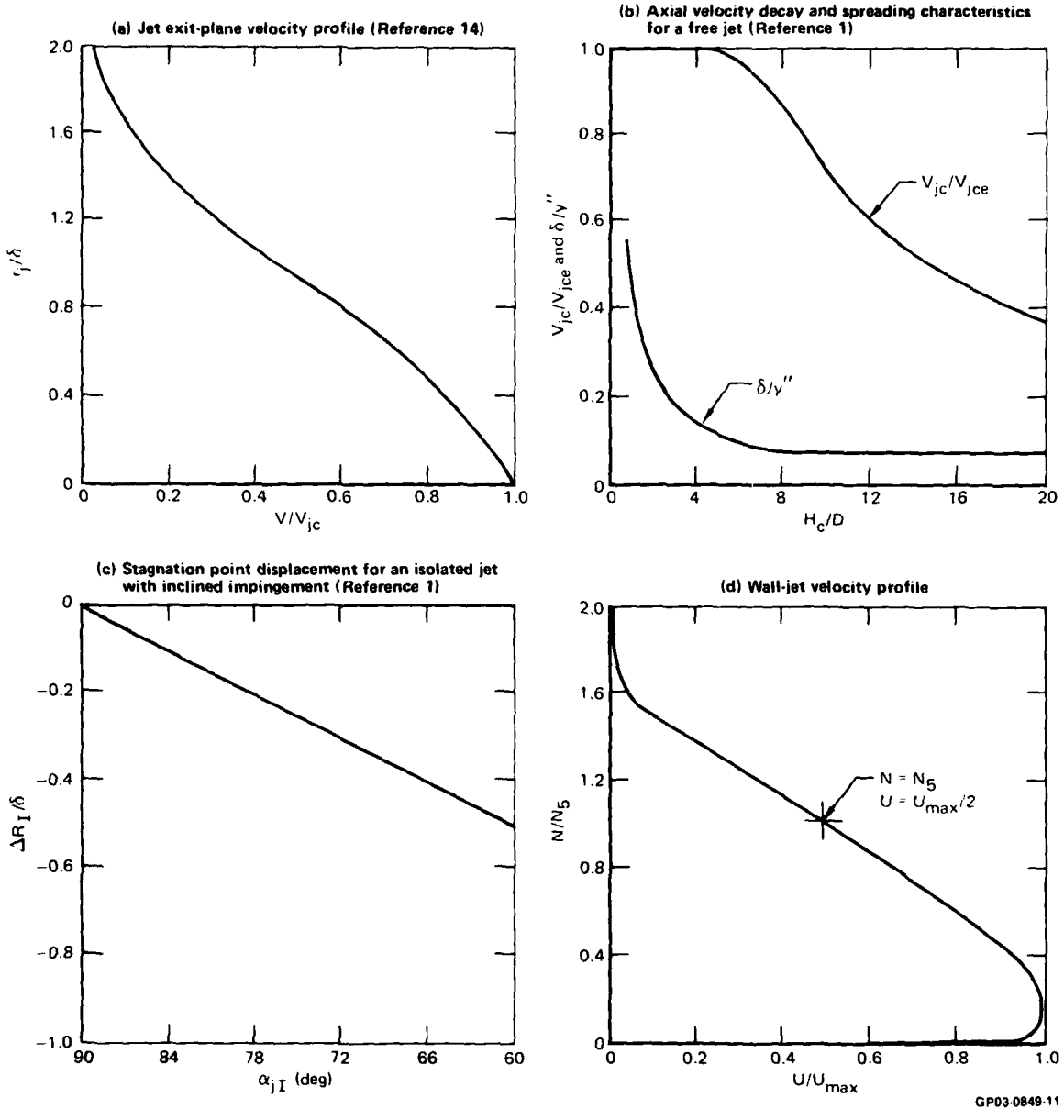

Figure 18. Empirical functions used in the specification of boundary conditions for the three-dimensional jet impingement configurations.

The geometric centerlines of the two nozzles intercept the top surface of the computational domain at the following distances from the nozzle exit planes:

$$y''_{h,1} = H_1 - \frac{h}{\sin \alpha_{jI}} \tag{A-4}$$

$$y''_{h,2} = H_2 - \frac{h}{\sin \alpha_{jI}} . \tag{A-5}$$

Using the data of Figure 18(b), the values of $V_{jch,1}$, $\delta_{h,1}$, $V_{jch,2}$, and $\delta_{h,2}$ are computed. The required velocity components at the top surface of the computational domain are then evaluated, completing the definition of the inflow velocity profiles through the primary jets.

Second, consider the specification of the velocity profiles in the exiting wall jets at the side surfaces of the computational domain, $z = -\frac{L}{2}$, $z = \frac{L}{2}$, and $x = w$. It is first necessary to define the origins from which the wall jets emanate. As pointed out by Jenkins and Hill in Reference 10, the impingement of an inclined jet on a ground plane produces a wall jet in which the flow properties depend on both radial distance from the origin and azimuthal orientation. If ϕ denotes the angular measurement around the jet impact point on the ground plane, $\phi = 0$ is defined as the orientation of maximum velocity on the ground plane. Donaldson and Snedeker, Reference 13, have shown that for oblique jet impingement, the maximum pressure point on the ground plane is displaced away from the jet centerline in the direction $\phi = 180^{\circ}$. The shifted stagnation point represents the effective origin of the wall-jet flow that is described by the coordinates r and ϕ. The magnitude of this displacement, denoted by ΔR_I, depends on both jet inclination angle and distance from the jet exit to the ground. In the present analysis, $\Delta R_I/\delta_I$ as a function of α_{jI} is computed using the curve of Donaldson and Snedeker which is reproduced in Figure 18(c).

With the origin of the wall jet established, the wall-jet velocity profile is defined using the methodology presented in Reference 1. The maximum wall-jet velocity at the edge of the impingement region, U_{max_I}, is related to V_{jc_I} by

$$U_{max_I} = V_{jc_I} \left[0.55 + 0.170 \left(\frac{90^o - \alpha_{jI}}{15^o}\right)\right]$$

$$\times \left[1.0 - 0.4 \left(\frac{90^o - \alpha_{jI}}{15^o}\right) \sin \frac{\phi}{2}\right] . \qquad \text{(A-6)}$$

V_{jc_I} is determined from the curve of Figure 18(b). The behavior of U_{max} with r follows the characteristic radial decay,

$$U_{max}(r) = \frac{R_I}{r} U_{max_I}, \qquad \text{(A-7)}$$

where R_I is evaluated from the correlation

$$R_I = 4.8\ \delta_I. \qquad \text{(A-8)}$$

δ_I follows from the curve of Figure 18(b). Knowing U_{max} at the required points on the outflow boundaries, a polynomial curve fit to the characteristic wall-jet velocity profile shown in Figure 18(d) is used to compute the velocity profile as a function of N/N_5. N denotes the normal distance above the ground plane, and N_5 denotes the value at which $U = 0.5\ U_{max}$. N_5, a function of r, is computed from

$$N_5\ (r) = N_{5_I} + 0.07\ (r - R_I), \qquad \text{(A-9)}$$

with N_{5_I} evaluated from a mass balance given in Reference 1. Equations (A-6) through (A-9) are used to compute the wall-jet velocity profiles resulting from each of the primary jets, and the projections of U at the required points on the outflow planes are computed.

The final step is to compute the velocity profiles through the fountain on the computational domain boundaries y = h and x = w. This step requires

calculation of the intersection of the fountain with these planes, a computation which begins with the determination of the fountain stagnation-line displacement on the ground plane. The distance from the origin of wall jet 1 to the point where the opposing wall jets collide is given by

$$r_{1,s} = \Delta R_{I,1} + \frac{S}{2 \sin \alpha_{jI}} + z_o' . \tag{A-10}$$

Similarly, the distance from the origin of wall jet 2 to the collision line is

$$r_{2,s} = \frac{S}{2 \sin \alpha_{jI}} - \Delta R_{I,2} - z_o' . \tag{A-11}$$

In the previous equations, z_o' represents the displacement of the fountain stagnation line from the midpoint of the distance between the intercepts of the geometric nozzle centerlines and the ground plane. Using Equation (A-7) and the condition that the wall-jet velocities are equal at the collision line, it follows that

$$\frac{R_{I,1}}{r_{1,s}} U_{max_{I,1}} = \frac{R_{I,2}}{r_{2,s}} U_{max_{I,2}} . \tag{A-12}$$

The combination of Equations (A-10) through (A-12) gives

$$z_o' = \frac{f_2(\alpha_{jI}) - \dfrac{R_{I,2}\, U_{max_{I,2}}}{R_{I,1}\, U_{max_{I,1}}} f_1(\alpha_{jI})}{\dfrac{R_{I,2}\, U_{max_{I,2}}}{R_{I,1}\, U_{max_{I,1}}} + 1} , \tag{A-13}$$

where

$$f_1(\alpha_{jI}) = \Delta R_{I,1} + \frac{S}{2 \sin \alpha_{jI}} \tag{A-14}$$

and

$$f_2(\alpha_{jI}) = \frac{S}{2 \sin \alpha_{jI}} - \Delta R_{I,2} \, . \tag{A-15}$$

Consider the velocity ratio $U_{max_{I,2}}/U_{max_{I,1}}$ in Equation (A-13). Wall jet 1 approaches the stagnation line with $\phi = 0$, and wall jet 2 approaches the stagnation line with $\phi = 180^{o}$. Therefore, from Equation (A-6),

$$\frac{U_{max_{I,2}}}{U_{max_{I,1}}} = \frac{V_{jcI,2}}{V_{jcI,1}} \left[1.0 - 0.4 \left(\frac{90^{o} - \alpha_{jI}}{15^{o}} \right) \right] . \tag{A-16}$$

Equation (A-14) in conjunction with Equation (A-13) provides the displacement of the stagnation line.

The next step is to compute the inclination of the fountain. Using conservation of momemtum principles and the approximation that the upwash can be treated as a radial planar flow, it can be shown in an analysis analogous to that given in Reference 10 that the upwash inclination Θ is related to the ratio of the wall-jet thicknesses in the following manner:

$$\Theta = \sin^{-1} \left(\frac{\tau - 1}{\tau + 1} \right), \tag{A-17}$$

where

$$\tau = \frac{N_{5I,1} + 0.07 \, [f_1 (\alpha_{jI}) + z_o' - R_{I,1}]}{N_{5I,2} + 0.07 \, [f_2 (\alpha_{jI}) - z_o' - R_{I,2}]} \, . \tag{A-18}$$

With the geometry of the fountain established, the velocity profiles can be computed on planes passing through the fountain which are the boundaries of the computational domain. Following the analysis of Jenkins and Hill, Reference 10, the maximum upwash velocity W_{max} at a specified value of y for x = 0 is given by

$$\frac{W_{max_o}}{V_{jce,1}} = \left(\frac{P_s - P_A}{q_{j,1}}\right)^{1/2} \left(\frac{\Delta R_{I,1} + \frac{S}{2 \sin \alpha_{jI}} + z_o' + y'}{\Delta R_{I,1} + \frac{S}{2 \sin \alpha_{jI}} + z_o'}\right)^{-1.6}, \qquad \text{(A-19)}$$

where P_s is the surface pressure at the stagnation line, P_A is the ambient pressure, and $q_{j,1}$ is the dynamic pressure at the jet exit. The pressure coefficient term is evaluated from an empirical correlation. The maximum local velocity in the upwash is assumed to have the following variation with radial distance from the virtual origin:

$$W_{max}(r_u) = \frac{R_o}{r_u} W_{max_o}, \qquad \text{(A-20)}$$

where

$$R_o = \Delta R_{I,1} + \frac{S}{2 \sin \alpha_{jI}} + z_o' + y' \qquad \text{(A-21)}$$

and

$$r_u = \left[\left(\Delta R_{I,1} + \frac{S}{2 \sin \alpha_{jI}} + z_o' + y'\right)^2 + x^2\right]^{1/2}. \qquad \text{(A-22)}$$

Therefore,

$$\frac{W_{max}(r_u)}{W_{max_o}} = \frac{\Delta R_{I,1} + \frac{S}{2 \sin \alpha_{jI}} + z_o' + y'}{\left[\left(\Delta R_{I,1} + \frac{S}{2 \sin \alpha_{jI}} + z_o' + y'\right)^2 + x^2\right]^{1/2}} . \quad \text{(A-23)}$$

Finally, the velocity variation normal to the upwash plane, $W(r_u, \xi)$, is computed, where ξ denotes a coordinate perpendicular to this plane passing through r_u. The assumption is made that the profile has the Gaussian form given in Reference 15,

$$\frac{W(r_u, \xi)}{W_{max}(r_u)} = \exp\left[-0.693(\xi/\xi_{0.25})^2\right]. \quad \text{(A-24)}$$

In this equation $\xi_{0.25}$ represents the distance from the center of the upwash to the half-velocity point of the profile and is computed from the following relationship:

$$\xi_{0.25} = \frac{1}{12}\left[\left(\Delta R_{I,1} + \frac{S}{2 \sin \alpha_{jI}} + z_o' + y'\right)^2 + x^2\right]^{1/2} . \quad \text{(A-25)}$$

Substitution of Equation (A-24) into Equation (A-23) yields

$$\frac{W(r_u; \xi)}{W_{max_o}} = \frac{\left(\Delta R_{I,1} + \frac{S}{2 \sin \alpha_{jI}} + z_o' + y'\right) \exp\left[-0.693(\xi/\xi_{0.25})^2\right]}{\left[\left(\Delta R_{I,1} + \frac{S}{2 \sin \alpha_{jI}} + z_o' + y'\right)^2 + x^2\right]^{1/2}} \quad \text{(A-26)}$$

The required components of the velocity profiles normal to the outflow planes are obtained using simple geometric relationships. The velocity variation over the remainder of the top surface of the computational domain is computed using an integral mass balance in which the difference between the outflow and

inflow of mass is taken to be the mass entrained. The latter is distributed uniformly outside the primary jets and fountain and is used to evaluate the entrainment velocity distribution.

The specification of the boundary conditions is simplified for the case of two jets with normal impingement. In this configuration (illustrated in Figure 2-(a)), two additional symmetry planes comprise the boundaries of the computational domain, and the wall-jet velocity distribution need be calculated on only a single outflow plane.

It should be emphasized that the numerical solution scheme for the time-averaged Navier-Stokes equations described in Section 3.0 is not limited to the boundary conditions given in this appendix. As improvements are made in the engineering approximations used to define the boundary values of the normal velocity components, the corresponding changes in boundary conditions need be made in only one routine of the computer code.

APPENDIX B: CENTRAL-DIFFERENCE FORMULAS USED IN THE FINITE-DIFFERENCE SOLUTION OF THE GOVERNING EQUATIONS

In the numerical solution scheme described in Section 3.0, central-difference approximations to the following derivatives of ϕ (an arbitrary flow variable) are required:

$$\frac{\partial \phi}{\partial x}, \frac{\partial^2 \phi}{\partial x^2}, \frac{\partial^2 \phi}{\partial x \partial y}, \frac{\partial \phi}{\partial y}, \frac{\partial^2 \phi}{\partial y^2}, \frac{\partial^2 \phi}{\partial y \partial z}, \frac{\partial \phi}{\partial z}, \frac{\partial^2 \phi}{\partial z^2}, \text{ and } \frac{\partial^2 \phi}{\partial x \partial z} .$$

The approximate forms of these derivatives are derived using a Taylor-series expansion and retaining a sufficient number of terms to ensure that each approximating formula is accurate to $O(h^2)$, where h is the finite-difference node spacing in all three coordinate directions. Different formulas are required for the interior region, the boundary planes, and the corners of the computational domain. Representative formulas for derivatives with respect to x are given below for the interior, the boundary plane i = 1, and the lower corner i = 1, j = 1 of the nodal network. Analogous formulas apply to the boundary plane i = I and the remaining corners and to the derivatives with respect to y and z. The notation used in the following finite-difference approximations is defined in Figure 3.

$$\left.\frac{\partial \phi}{\partial x}\right|_{i,j,k} = \frac{\phi_{i+1,j,k} - \phi_{i-1,j,k}}{2h} \quad \text{(interior point)} \tag{B-1}$$

$$\left.\frac{\partial \phi}{\partial x}\right|_{1,j,k} = \frac{4\phi_{2,j,k} - \phi_{3,j,k} - 3\phi_{1,j,k}}{2h} \quad \text{(boundary point, i = 1)} \tag{B-2}$$

$$\left.\frac{\partial^2 \phi}{\partial x^2}\right|_{i,j,k} = \frac{\phi_{i+1,j,k} - 2\phi_{i,j,k} + \phi_{i-1,j,k}}{h^2} \quad \text{(interior point)} \tag{B-3}$$

$$\left.\frac{\partial^2\phi}{\partial x^2}\right|_{1,j,k} = \frac{4\phi_{3,j,k} - \phi_{4,j,k} - 5\phi_{2,j,k} + 2\phi_{1,j,k}}{h^2}$$

(boundary point, i = 1) (B-4)

$$\left.\frac{\partial^2\phi}{\partial x\partial y}\right|_{i,j,k} = \frac{\phi_{i+1,j+1,k} - \phi_{i-1,j+1,k} + \phi_{i-1,j-1,k} - \phi_{i+1,j-1,k}}{4h^2}$$

(interior point) (B-5)

$$\left.\frac{\partial^2\phi}{\partial x\partial y}\right|_{1,j,k} = \left[4\phi_{2,j+1,k} - 4\phi_{2,j-1,k} - \phi_{3,j+1,k} + \phi_{3,j-1,k} - 3\phi_{1,j+1,k} + 3\phi_{1,j-1,k}\right]/4h^2$$

(boundary point, i = 1) (B-6)

$$\left.\frac{\partial^2\phi}{\partial x\partial y}\right|_{1,1,k} = \left[16\phi_{2,2,k} - 4\phi_{2,3,k} - 12\phi_{2,1,k} - 4\phi_{3,2,k} + \phi_{3,3,k} + 3\phi_{3,1,k} - 12\phi_{1,2,k} + 3\phi_{1,3,k} + 9\phi_{1,1,k}\right]/4h^2$$

(corner point, i = 1 and j = 1) (B-7)

The derivative formulas are stored on a library tape which is accessed by the computer codes used to solve the finite-difference equations.

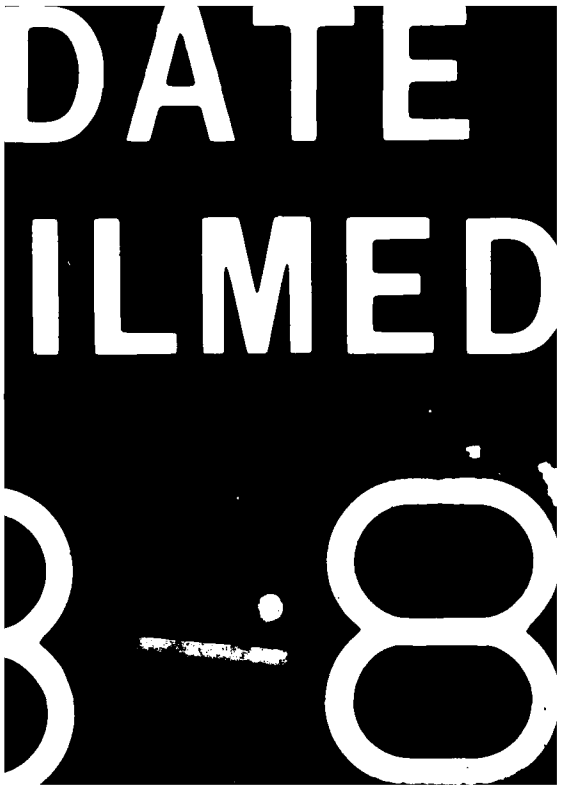
DATE
ILMED
8